Revealing unexpected complex encoding but simple decoding mechanisms in motor cortex via separating task-relevant neural signals

Yangang Li[1,2,4], **Xinyun Zhu**[1,2,4], **Yu Qi**[3,4] †, **Yueming Wang**[1,5] †

[1] Qiushi Academy for Advanced Studies, Zhejiang University, Hangzhou, China
[2] College of Computer Science and Technology, Zhejiang University, Hangzhou, China
[3] Affiliated Mental Health Center & Hangzhou Seventh People's Hospital and the MOE Frontier Science Center for Brain Science and Brain-machine Integration, Zhejiang University School of Medicine, Hangzhou, China
[4] The State Key Lab of Brain-Machine Intelligence, Zhejiang University, Hangzhou, China
[5] Zhejiang Brain-Computer Interface Institute, Hangzhou, China

Abstract. In motor cortex, task-relevant neural responses are entangled with irrelevant signals, which complicates the study of encoding and decoding mechanisms. It remains unclear whether task-irrelevant signals could conceal some critical truth. One solution is to accurately separate task-relevant and irrelevant signals, but this approach remains elusive due to the unknown ground truth of task-relevant signals. Therefore, we propose a framework to define, extract, and validate task-relevant signals. Analyzing separated signals in three monkeys performing different reaching tasks, we found neural responses previously considered useless encode rich task information in complex nonlinear ways. These responses are critical for neuronal redundancy and reveal movement behaviors occupy a higher-dimensional neural space than previously expected. Surprisingly, when incorporating often-ignored neural dimensions, task information can be decoded linearly as accurately as nonlinear decoding, suggesting linear readout is performed in motor cortex. Our findings prompt that separating task-relevant signals may help uncover more hidden cortical mechanisms.

† Corresponding authors: Yu Qi (qiyu@zju.edu.cn) and Yueming Wang (ymingwang@zju.edu.cn).

1. Introduction

Understanding how motor cortex encodes and decodes movement behaviors is a fundamental goal of neuroscience [1, 2]. However, achieving this goal faces significant challenges because task-relevant neural responses are entangled with task-irrelevant factors such as responses for other task variables [3,4] and ongoing noise [5,6]. Generally, irrelevant signals would hinder the accurate investigation of the relationship between neural activity and tasks. This raises concerns about whether irrelevant signals could conceal some critical facts about neural encoding and decoding mechanisms.

If the answer is yes, a natural question arises: what critical facts about neural encoding and decoding would irrelevant signals conceal? In terms of neural encoding, irrelevant signals may mask some small neural components, making their encoded information difficult to detect [7], thereby misleading us to neglect the role of these signals, leading to a partial understanding of neural mechanisms. For example, at the single-neuron level, weakly-tuned neurons are often assumed useless and not analyzed [8–11]; at the population level, neural signals composed of lower variance principal components (PCs) are typically treated as noise and discarded [12–15]. So are these ignored signals truly useless or appear that way only due to being covered by irrelevant signals? And what's the role of these ignored signals? In terms of neural decoding, irrelevant signals would significantly complicate the information readout [16, 17], potentially hindering the discovery of the true readout mechanism of task-relevant responses. Specifically, in motor cortex, in what form (linear or nonlinear) downstream neurons read out task information from neural responses is an open question. The linear readout is biologically plausible and widely used [8–10], but recent studies [18, 19] demonstrate nonlinear readout outperforms linear readout. So which readout scheme is more likely to be used by the motor cortex? Whether irrelevant signals are the culprits for the performance gap? Unfortunately, the above issues remain unclear.

One approach to address the above issues is to accurately separate task-relevant and irrelevant signals at the single-neuron level and then analyze noise-free task-relevant signals, which enables us to gain a more accurate and comprehensive understanding of the underlying neural mechanisms. However, this approach is hampered by the fact that the ground truth of task-relevant signals is unknown, which makes the definition, extraction, and validation of task-relevant signals a challenging task. As a result, methods of accurate separation remain elusive to date. Existing methods for extracting task-relevant patterns mainly focus on the latent population level [12,20–23] rather than the single-neuron level, and they extract neural activities based on assumptions about specific neural properties, such as linear or nonlinear dynamics [20, 21]. Although these methods have shown promising results, they fail to capture other task-relevant neural activities that do not meet their assumptions, thereby providing an incomplete picture of task-relevant neural activity. To overcome these limitations and obtain accurate task-relevant signals at the single-neuron level, we propose a novel framework that

defines, extracts, and validates task-relevant signals by simultaneously considering such signals' encoding (task-relevant signals should be similar to raw signals to preserve the underlying neuronal properties) and decoding (task-relevant signals should contain task information as much as possible) properties (see Methods and Fig. 1). This framework establishes a prerequisite foundation for the subsequent detailed analysis of neural mechanisms.

Here, we conducted experiments using datasets recorded from the motor cortex of three monkeys performing different reaching tasks. After signal separation by our approach, we first explored how the presence of task-irrelevant signals affect the analysis of neural activity. We found that task-irrelevant signals account for a large amount of trial-to-trial neuronal variability, and are evenly distributed across the neural dimensions of task-relevant signals. Then we explored whether irrelevant signals conceal some facts of neural encoding and decoding. For neural encoding, irrelevant signals obscure the task information encoded by neural responses, especially for neural responses with a large degree of nonlinearity. Surprisingly, neural responses that are usually ignored (weakly-tuned neurons and neural signals composed of small variance PCs) actually encode rich task information in complex nonlinear ways. These responses underpin an unprecedented neuronal redundancy and reveal that movement behaviors are distributed in a higher-dimensional neural space than previously thought. For neural decoding, irrelevant signals complicate information readout. Strikingly, when uncovering small neural components obscured by irrelevant signals, linear decoders can achieve comparable decoding performance with nonlinear decoders, providing strong evidence for the presence of linear readout in motor cortex. Together, our findings reveal unexpected complex encoding but simple decoding mechanisms in the motor cortex. Finally, our study also has implications for developing accurate and robust brain-machine interfaces (BMIs) and, more generally, provides a powerful framework for separating task-relevant and irrelevant signals, which can be applied to other cortical data to uncover more neural mechanisms masked by task-irrelevant signals.

2. Results

2.1. Framework for defining, extracting, and validating task-relevant neural signals

2.1.1. What are task-relevant neural signals. Since the ground truth of task-relevant signals is unknown, the definition of task-relevant signals is not well established yet. In this study, we propose that task-relevant signals should meet two requirements: (1) they should be similar to raw signals in order to preserve the underlying neuronal properties (encoding requirement), and (2) they should contain task information as much as possible (decoding requirement). If the signals meet both of these requirements, we consider them to be effective task-relevant signals.

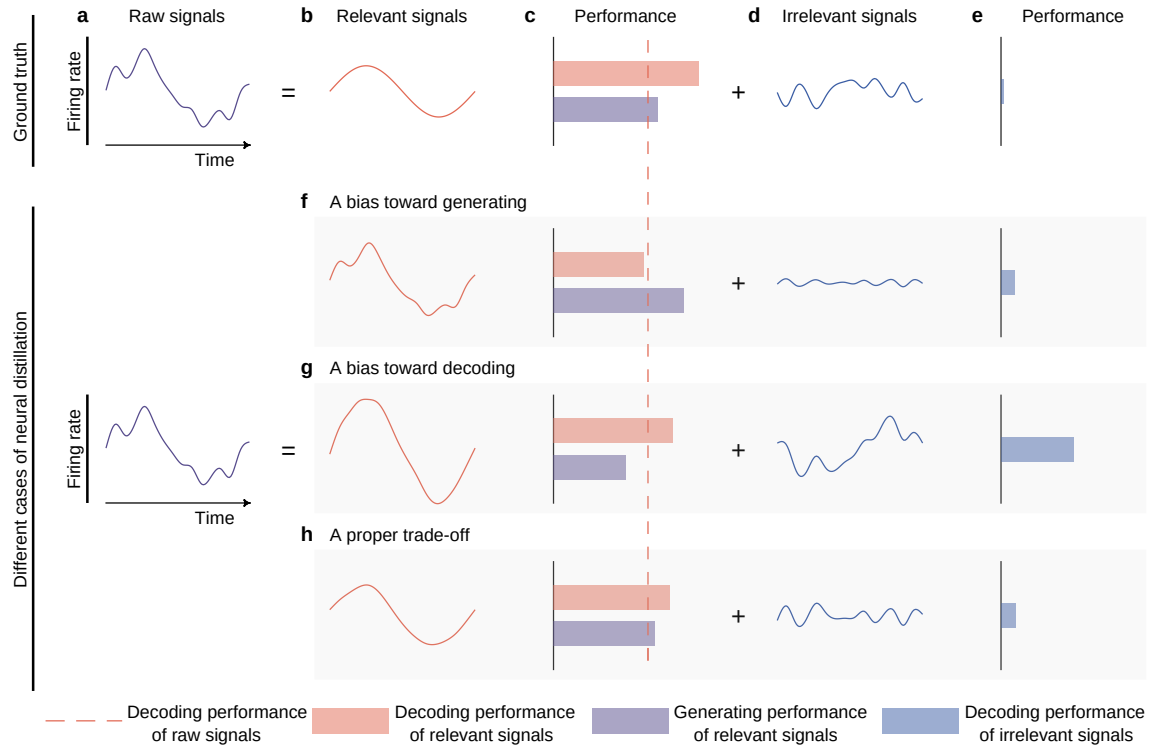

Figure 1: **Semantic illustration of extracting and validating task-relevant signals. a-e** The ideal decomposition of raw signals. **a**, The temporal neuronal activity of raw signals, where x-axis denotes time, and y-axis represents firing rate. Raw signals are decomposed to relevant (**b**) and irrelevant (**d**) signals. The red dotted line indicates the decoding performance of raw signals. The red and blue bars represent the decoding performance of relevant and irrelevant signals. The purple bar represents the generating performance of task-relevant signals, which measures the neural similarity between generated signals and raw signals. The longer the bar, the larger the performance. The ground truth of relevant signals decode information perfectly (**c**, red bar) and is similar to raw signals to some extent (**c**, purple bar), and the ground truth of irrelevant signals contain little task information (**e**, blue bar). **f-h**, Three different cases of task-relevant signals distillation. **f**, When the model is biased toward generating task-relevant signals that are similar to raw signals, it will achieve high generating performance, but the decoding performance will suffer due to the inclusion of too many irrelevant signals. As it is difficult for models to extract complete task-relevant signals, the residuals will also contain some task information. **g**, When the model is biased toward generating signals that prioritize decoding over similarity to raw signals, it will achieve high decoding performance, but the generating performance will be low. Meanwhile, the residuals will contain a significant amount of task information. **h**, When the model balances the trade-off of decoding and generating capabilities of relevant signals, both decoding and generating performance will be good, and the residuals will only contain a little task information.

2.1.2. How to extract task-relevant signals. One way to extract task-relevant signals is to use a distillation model to generate them from raw signals, while considering the remaining signals as task-irrelevant. However, due to the unknown ground truth of task-relevant signals, a key challenge for the model is to determine the optimal degree of similarity between the generated signals and raw signals. If the generated signals are too similar to raw signals, they may contain a large amount of task-irrelevant information, which would hinder the exploration of neural mechanisms. Conversely, if the generated signals are too dissimilar to raw signals, they may lose task-relevant information, also hindering the exploration of neural mechanisms. To overcome this challenge, we exploited the trade-off between the similarity of generated signals to raw signals (encoding requirement) and their decoding performance of tasks (decoding requirement) to extract effective task-relevant signals (for details, see Methods). The core assumption of our model is that task-irrelevant signals are noise relative to task-relevant signals, and thereby irrelevant signals would degrade the decoding generalization of generated task-relevant signals. Generally, the distillation model is faced with three cases: a bias toward generating (Fig. 1f), a bias toward decoding (Fig. 1g), and a proper trade-off (Fig. 1h). If the distillation model is biased toward extracting signals similar to raw signals, the distilled task-relevant signals will contain an excessive amount of task-irrelevant information, affecting the decoding generalization of these signals (Fig. 1f). If the model is biased toward extracting parsimonious signals that are discriminative for decoding, the distilled signals will not be similar enough to raw signals, and some redundant but useful signals will be left in the residuals (Fig. 1g). Neither of these two cases is desirable because the former loses decoding performance, while the latter loses some useful neural signals, which are not conducive to our subsequent analysis of the relationship between task-relevant signals and tasks. The task-relevant signals we want should be similar to raw signals and preserve the task information maximally, which can be obtained by balancing the encoding and decoding properties of generated task-relevant signals (Fig. 1h).

2.1.3. How to validate task-relevant signals. To validate the effectiveness of the distilled signals, we proposed three criteria. The first criterion is that the decoding performance of the task-relevant signals (red bar, Fig.1) should surpass that of raw signals (the red dotted line, Fig.1). Since decoding models, such as deep neural networks, are more prone to overfit noisy raw signals than task-relevant signals, the distilled signals should demonstrate better decoding generalization than the raw signals. The second criterion is that the task-irrelevant signals should contain minimal task information (blue bar, Fig.1). This criterion can assess whether the distilled signals maximally preserve task information from the opposite perspective and effectively exclude undesirable cases, such as over-generated and under-generated signals. Specifically, in the case of over-generation, suppose $z = x + y$, where z, x, and y represent raw, relevant, and irrelevant signals, respectively. If the distilled relevant signals $\hat{x}$ are added extra signals m which do not exist in the real task-relevant signals, that is, $\hat{x} = x + m$, then the corresponding

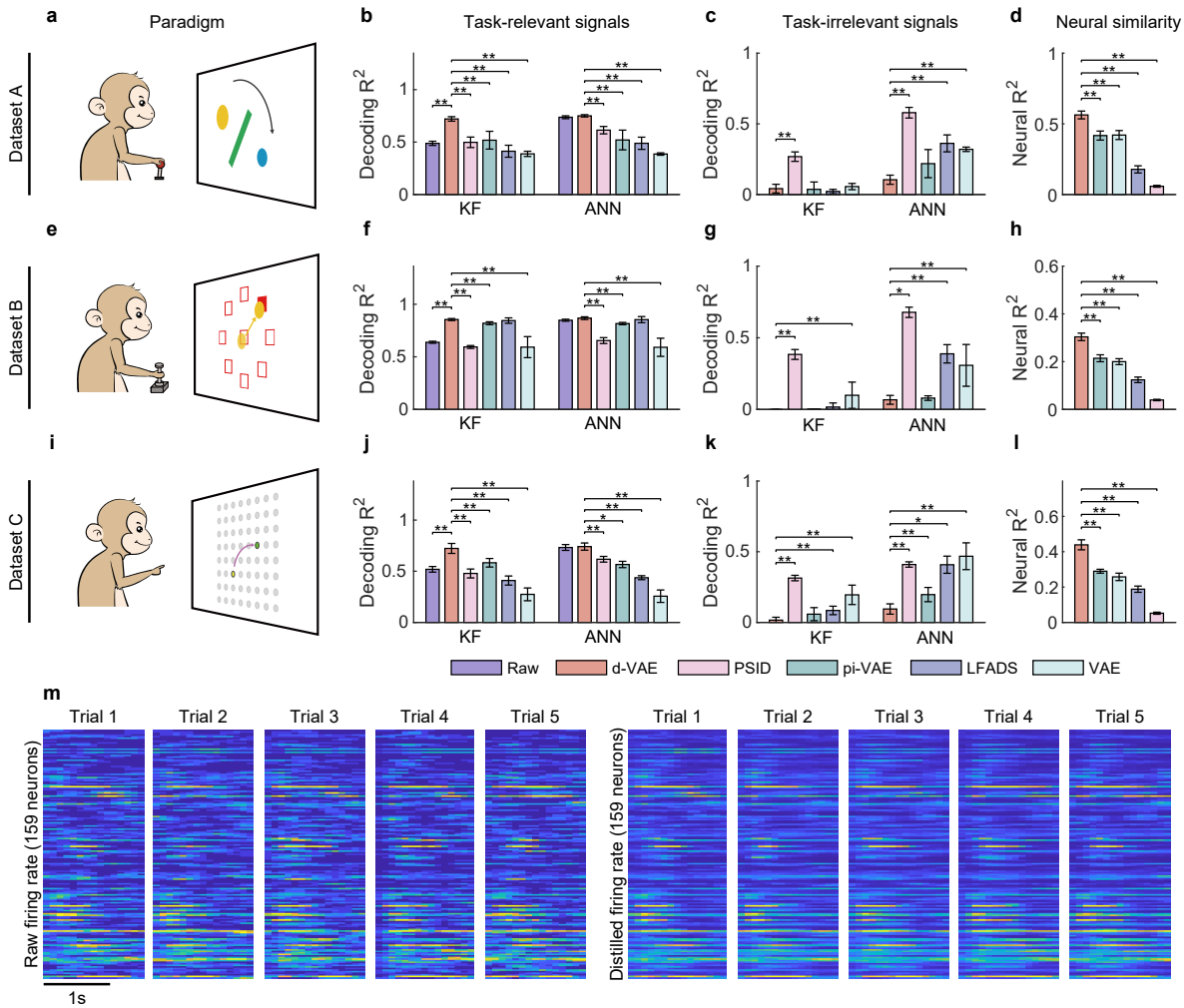

Figure 2: **Evaluation of separated signals.** **a**, The obstacle avoidance paradigm **b**, The decoding R^2 between true velocity and predicted velocity of raw signals and task-relevant signals obtained by d-VAE, PSID, pi-VAE, LFADS, and VAE on dataset A. Error bars denote mean ± standard deviation (s.d.) across five cross-validation folds. Asterisks represent significance of Wilcoxon rank-sum test with $^{\star}P < 0.05$, $^{\star\star}P < 0.01$. **c**, Same as **b**, but for task-irrelevant signals obtained by five different methods. **d**, The neural similarity (R^2) between raw signals (purple) and task-relevant signals extracted by d-VAE (red), PSID (pink), pi-VAE (green), LFADS (blue), and VAE (light green). Error bars represent mean ± s.d. across five cross-validation folds. Asterisks indicate significance of Wilcoxon rank-sum test with $^{\star\star}P < 0.01$. **e-h** and **i-l**, Same as **a-d**, but for dataset B with the center-out paradigm (**e**) and dataset C with the self-paced reaching paradigm (**i**). **m**, The firing rates of raw signals and distilled signals obtained by d-VAE in five held-out trials under the same condition of dataset B.

residuals $\hat{y}$ will be equal to the ideal irrelevant signals z plus the negative extra signals $-m$, namely, $\hat{y} = y - m$, thus the residuals $\hat{y}$ contain the amount of information

preserved by negative extra signals $-m$. Similarly, in the case of under-generation, if the distilled task-relevant signals are incomplete and lose some useful information, this lost information will also be reflected in the residuals. In these cases, the distilled signals are not suitable for analysis. The third criterion is that the distilled task-relevant signals should be similar to raw signals to maintain essential neuronal properties (purple bar, Fig.1). If the distilled signals do not resemble raw signals, they will not retain the critical characteristics of raw signals, which are not qualified for subsequent analysis. Overall, if the distilled signals satisfy the above three criteria, we consider the distilled signals to be effective.

2.2. d-VAE extracts effective task-relevant signals

To demonstrate the effectiveness of our model (d-VAE) in extracting task-relevant signals, we conducted experiments on three benchmark datasets with different paradigms (Fig. 2a,e,i; see Methods for details), and compared d-VAE with four other distillation models, including pi-VAE [23], PSID [20] and LFADS [21], and a vanilla VAE [24]. Specifically, we first applied these distillation models to raw signals to obtain the distilled task-relevant signals, considering the residuals as task-irrelevant signals. We then evaluated the decoding R^2 between the predicted velocity and actual velocity of the two partition signals using a linear Kalman filter (KF) and a nonlinear artificial neural network (ANN) and measured the neural similarity between task-relevant and raw signals.

Overall, d-VAE successfully extracts effective task-relevant signals that meet the three criteria outlined in Section 2.1.3. In the obstacle avoidance task (Fig. 2a), the monkey is required to move the ball from the start point (yellow) to the target point (blue) without hitting the obstacle. For the decoding performance of task-relevant signals (Fig. 2b), the signals distilled by d-VAE outperform the raw signals (purple) and the signals distilled by all other distillation models (PSID, pink; pi-VAE, green; LFADS, blue; and VAE, light green) with the KF as well as the ANN. For the decoding performance of task-irrelevant signals (Fig. 2c), task-irrelevant signals obtained by d-VAE achieves the lowest decoding performance compared with task-irrelevant signals obtained by other approaches. Therefore, the combination of dVAE's highest decoding performance for task-relevant signals and lowest decoding performance for task-irrelevant signals demonstrate its superior ability to extract task-relevant signals from noisy signals. For the neural similarity between task-relevant and raw signals (Fig. 2d), the distilled signals obtained by d-VAE achieve the highest performance among competitors ($P < 0.01$, Wilcoxon rank-sum test). Similar results were obtained for the center-out task (Fig. 2e-h) and the self-paced reaching task (Fig. 2i-l), indicating the consistency of d-VAE's distillation ability across a range of motor tasks. To provide a more intuitive illustration of the similarity between raw and distilled signals, we displayed the firing rate of neuronal activity in five trials under the same condition (Fig. 2m), and results clearly show that the firing pattern of distilled signals is similar

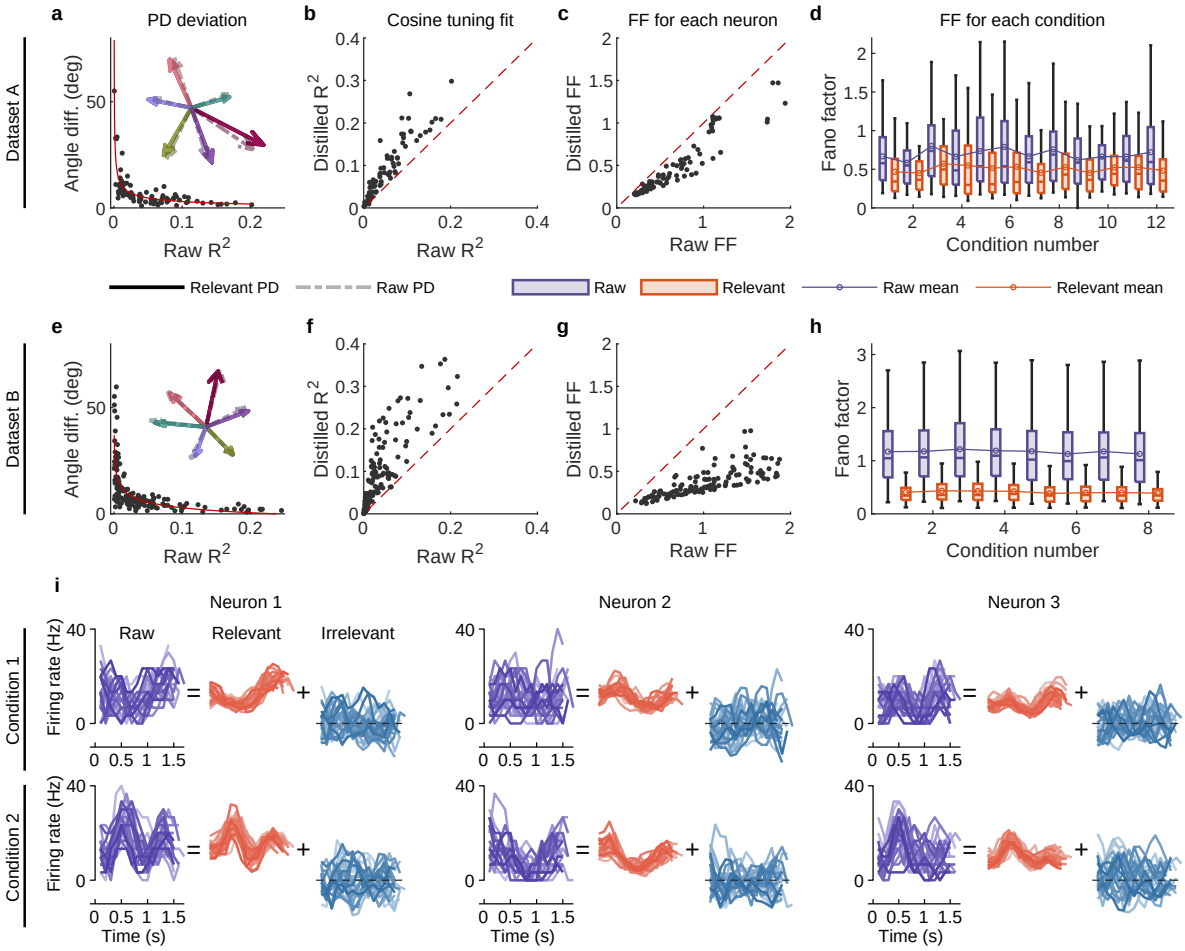

Figure 3: **The effect of irrelevant signals on analyzing neural activity at the single-neuron level.** **a**, The angle difference (AD) of preferred direction (PD) between raw and distilled signals as a function of the R^2 of raw signals on datasets A, where R^2 represents the proportion of neuronal activity explained by the linear encoding model. Each black point represents a neuron (n = 90). The red curve is the fitting curve between R^2 and AD. Five example larger R^2 neurons' PDs are shown in the inset plot, where the solid and dotted line arrows represent the PDs of relevant and raw signals, respectively. **b**, Comparison of the cosine tuning fit (R^2) before and after distillation of single neurons (black points), where the x-axis and y-axis represent neurons' R^2 of raw and distilled signals, respectively. **c**, Comparison of neurons' Fano factor (FF) averaged across conditions of raw (x-axis) and distilled (y-axis) signals, where FF is used to measure the neuronal variability of different trials in the same condition. **d**, Boxplots of raw (purple) and distilled (red) signals under different conditions for all neurons (12 conditions). Boxplots represent medians (lines), quartiles (boxes), and whiskers extending to ± 1.5 times the interquartile range. The broken lines represent the mean FF across all neurons. **e-h**, Same as **a-d**, but for dataset B (n=159, 8 conditions). **i**, Example of three neurons' raw firing activity decomposed into task-relevant and irrelevant parts using all trials under two conditions (2 of 8 directions) in held-out test sets of dataset B.

to the corresponding raw signals.

In summary, d-VAE distills effective task-relevant signals that preserve task information maximally and are similar to raw signals. Meanwhile, the task-irrelevant signals discarded by d-VAE contain a little task information. Therefore, these signals are reliable for exploring the encoding and decoding mechanisms of relevant signals.

2.3. How do task-irrelevant signals affect the analysis of neural activity at the single-neuron level?

Following signal separation, we first explored how task-irrelevant signals affect the analysis of neural activity at the single-neuron level. Specifically, we examined the effect of irrelevant signals on two critical properties of neuronal activity: the preferred direction (PD) [8] and trial-to-trial variability. Our objective was to know how irrelevant signals affect the PD of neurons and whether irrelevant signals contribute significantly to neuronal variability.

To explore how irrelevant signals affect the PD of neurons, we first calculated the PD of both raw and distilled signals separately and then quantified the PD deviation by the angle difference between these two signals. Results show that the PD deviation increases as the neuronal R^2 decreases (red curve, Fig. 3a,e and Supplementary Fig. S1a); neurons with larger R^2 (strongly-tuned neurons) exhibit stable PDs with signal distillation (see example PDs in the inset), while neurons with smaller R^2s (weakly-tuned neurons) show a larger PD deviation. These results indicate that irrelevant signals have a small effect on strongly-tuned neurons but a large effect on weakly-tuned neurons. One possible reason for the larger PD deviation in weakly-tuned neurons is that they have a lower degree of linear encoding but a higher degree of nonlinear encoding, and highly nonlinear structures are more susceptible to interference from irrelevant signals [25]. Moreover, after filtering out the task-irrelevant signals, the cosine tuning fit (R^2) of neurons increases ($P < 10^{-20}$, Wilcoxon signed-rank test; Fig. 3b,f and Supplementary Fig. S1b), indicating that irrelevant signals reduce the neurons' tuning expression. Notably, even after removing the interference of irrelevant signals, the R^2 of neurons remains relatively low. These results demonstrate that the linear encoding model only explains a small fraction of neural responses, and neuronal activity encodes task information in complex nonlinear ways.

To investigate whether irrelevant signals significantly contribute to neuronal variability, we compared the neuronal variability (measured with the Fano factor [26], FF) of relevant and raw signals. Results show that the condition-averaged FF of each neuron of distilled signals is lower than that of raw signals ($P < 10^{-20}$, Wilcoxon signed-rank test; Fig. 3c,g), and the mean (broken line) and median FFs of all neurons under different conditions are also significantly lower than those of raw signals ($P < 0.01$, Wilcoxon signed-rank test; Fig. 3d,h), indicating that irrelevant signals significantly contribute to neuronal variability. We then visualized the single-trial neuronal activity of example neurons under different conditions (Fig. 3i and Supplementary Fig. S2).

Results demonstrate that the patterns of relevant signals are more consistent and stable across different trials than raw signals, and the firing activity of irrelevant signals varies randomly. These results indicate that irrelevant signals significantly contribute to neuronal variability, and eliminating the interference of irrelevant signals enables us observe the changes in neural pattern more accurately.

2.4. How do task-irrelevant signals affect the analysis of neural activity at the population level?

The neural population structure is an essential characteristic of neural activity. Here, we examined how task-irrelevant signals affect the analysis of neural activity at the population level, including four aspects: (1) the population properties of relevant and irrelevant signals, (2) the subspace overlap relationship between the two signal components, (3) how the two partitions contribute to raw signals, and (4) the difference in population properties between raw and distilled signals.

To explore the population properties of relevant and irrelevant signals, we separately applied principal component analysis (PCA) on each partition to obtain the corresponding cumulative variance curve in a descending variance order. Our results show that the primary subspace (capturing the top 90% variance) of relevant signals (thick red line, Fig.4a,e and Supplementary Fig. S3a) is only explained by a few dimensions (7, 13, and 9 for each dataset), indicating that the primary part of task-relevant signals exists in a low-dimensional subspace. In contrast, the primary subspace of irrelevant signals (thick blue line, Fig. 4b,f and Supplementary Fig. S3b) requires more dimensions (46, 81, and 59). The variance distribution of task-irrelevant signals across dimensions (thick blue line, Fig. 4b,f and Supplementary Fig. S3b) is more even than task-relevant signals (thick red line, Fig. 4a,e and Supplementary Fig. S3a) but not as uniform as Gaussian noise $\mathcal{N}(\mathbf{0}, \mathbf{I})$ (thin gray line, Fig.4b,f and Supplementary Fig. S3b), indicating that irrelevant signals are not pure noise but rather bear some significant structure, which may represent information from other irrelevant tasks.

To investigate the subspace overlap between relevant and irrelevant signals, we calculated how many variances of irrelevant signals can be captured by relevant PCs by projecting irrelevant signals onto relevant PCs and vice versa [27–29](see Methods). We found that the variance of irrelevant signals increases relatively uniformly over relevant PCs (blue thin line, Fig. 4a,e and Supplementary Fig. S3a), like random noise's variance accumulation explained by relevant PCs (gray thin line, Fig. 4a,e and Supplementary Fig. S3a); similar results are observed for relevant signals explained by irrelevant PCs (red thin line, Fig. 4b,f and Supplementary Fig. S3b). These results indicate that relevant PCs can not match the informative dimensions of irrelevant signals and vice versa, suggesting the dimensions of task-relevant and irrelevant signals are unrelated. It is worth mentioning that the signals obtained by pi-VAE are in contrast to our findings. Its results show that a few relevant PCs can explain a considerable variance of irrelevant signals (thin red line, Supplementary Fig. S4b,f,j), which indicates that the relevant

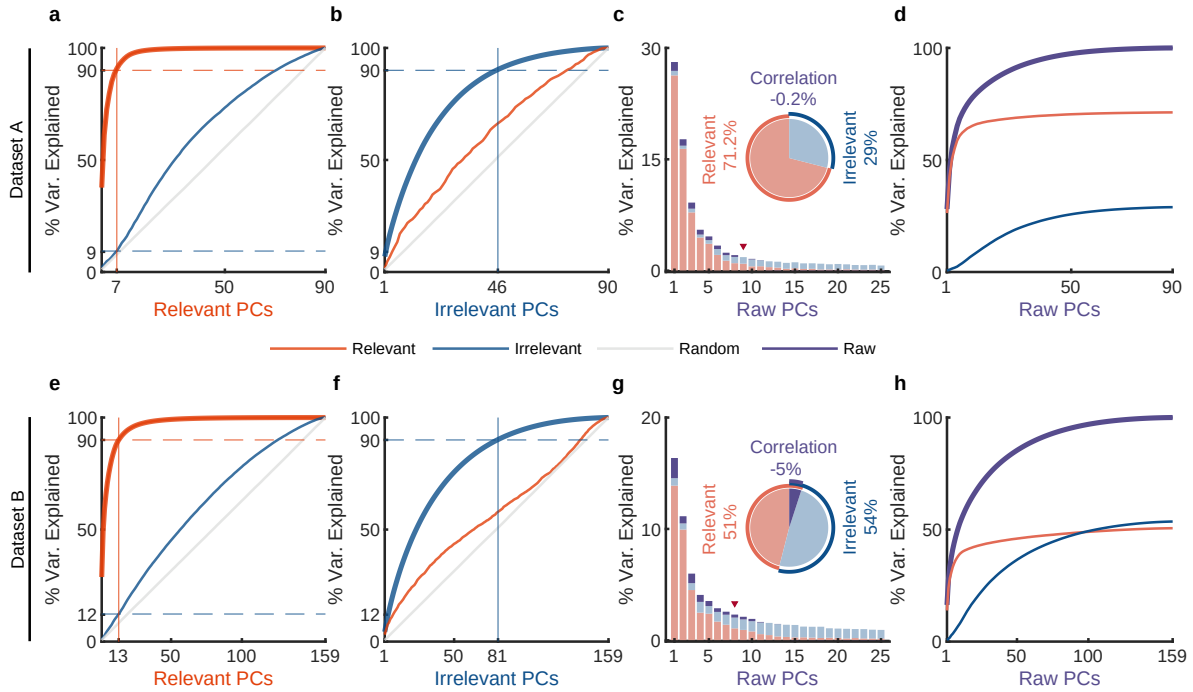

Figure 4: **The effect of irrelevant signals on analyzing neural activity at the population level. a,b**, PCA is separately applied on relevant and irrelevant signals to get relevant PCs and irrelevant PCs. The thick lines represent the cumulative variance explained for the signals on which PCA has been performed, while the thin lines represent the variance explained by those PCs for other signals. Red, blue, and gray colors indicate relevant signals, irrelevant signals, and random Gaussian noise $\mathcal{N}(\mathbf{0}, \mathbf{I})$ (for chance level) where the mean vector is zero and the covariance matrix is the identity matrix. The horizontal lines represent the percentage of variance explained. The vertical lines indicate the number of dimensions accounted for 90% of the variance in task-relevant (left) and irrelevant (right) signals. For convenience, we defined the principal component subspace describing the top 90% variance as the primary subspace and the subspace capturing the last 10% variance as the secondary subspace. The cumulative variance explained for task-relevant (**a**) and irrelevant (**b**) signals got by d-VAE on dataset A. **c,d**, PCA is applied on raw signals to get raw PCs. **c**, The bar plot shows the composition of each raw PC. The inset pie plot shows the overall proportion of raw signals, where red, blue, and purple colors indicate relevant signals, irrelevant signals, and the correlation between relevant and relevant signals. The PC marked with a red triangle indicates the last PC where the variance of relevant signals is greater than or equal to that of irrelevant signals. **d**, The cumulative variance explained by raw PCs for different signals, where the thick line represents the cumulative variance explained for raw signals (purple), while the thin line represents the variance explained for relevant (red) and irrelevant (blue) signals. **e-h**, Same as **a-d**, but for dataset B.

and irrelevant PCs are closely related. The possible reason is that the pi-VAE leaks a lot of information into the irrelevant signals. Notably, Fig. 4a,e and Supplementary Fig. S3a show that irrelevant signals got by d-VAE projecting on task-relevant primary subspace only capture a little variance information (9%, 12%, and 9%), indicating that the primary subspace of task-relevant signals is nearly orthogonal to irrelevant space.

To investigate the composition of raw signals by the two partitions, we performed PCA on raw neural signals to obtain raw PCs, and then projected the relevant and irrelevant signals onto these PCs to assess the proportion of variance of raw signals explained by each partition. First, we analyzed the overall proportion of relevant and irrelevant signals that constitute the raw signals (the inset pie plot, Fig. 4c,g and Supplementary Fig. S3c). The variance of the raw signals is composed of three parts: the variance of relevant signals, the variance of irrelevant signals, and the correlation between relevant and irrelevant signals (see Methods). The results demonstrate that the irrelevant signals account for a large proportion of raw signals, suggesting the motor cortex encodes considerable information that is not related to the measured behaviors. In addition, there is only a weak correlation between relevant and irrelevant signals, implying that task-relevant and irrelevant signals are nearly uncorrelated.

We then examined the proportions of relevant and irrelevant signals in each PC of raw signals. We found that relevant signals (red) occupy the dominant proportions in the larger variance raw PCs (before the PC marked with a red triangle), while irrelevant signals (blue) occupy the dominant proportions in the smaller variance raw PCs (after the PC marked with a red triangle) (Fig. 4c,g and Supplementary Fig. S3c). Similar results are observed in the accumulation of each raw PC (Fig. 4d,h and Supplementary Fig. S3d). Specifically, the results show that the variance accumulation of raw signals (purple line) in larger variance PCs is mainly contributed by relevant signals (red line), while irrelevant signals (blue line) primarily contribute to the lower variance PCs. These results demonstrate that irrelevant signals have a small effect on larger variance raw PCs but a large effect on smaller variance raw PCs. This finding eliminates the concern that irrelevant signals would significantly affect the top few PCs of raw signals and thus produce inaccurate conclusions. To further validate this finding, we used the top six PCs as jPCA [12] did to examine the rotational dynamics of distilled and raw signals (Fig. S5). Results show that the rotational dynamics of distilled signals are similar to those of raw signals.

Finally, to directly compare the population properties of raw and relevant signals, we plotted the cumulative variance curves of raw and relevant signals (Supplementary Fig. S6). Results (upper left corner curves, Supplementary Fig. S6) show that the cumulative variance curve of relevant signals (red line) accumulates faster than that of raw signals (purple line) in the preceding larger variance PCs, indicating that the variance of the relevant signal is more concentrated in the larger variance PCs than that of raw signals. Furthermore, we found that the dimensionality of primary subspace of raw signals (26, 64, and 45 for datasets A, B, and C) is significantly higher than that of task-relevant signals (7, 13, and 9), indicating that task-irrelevant signals lead to an

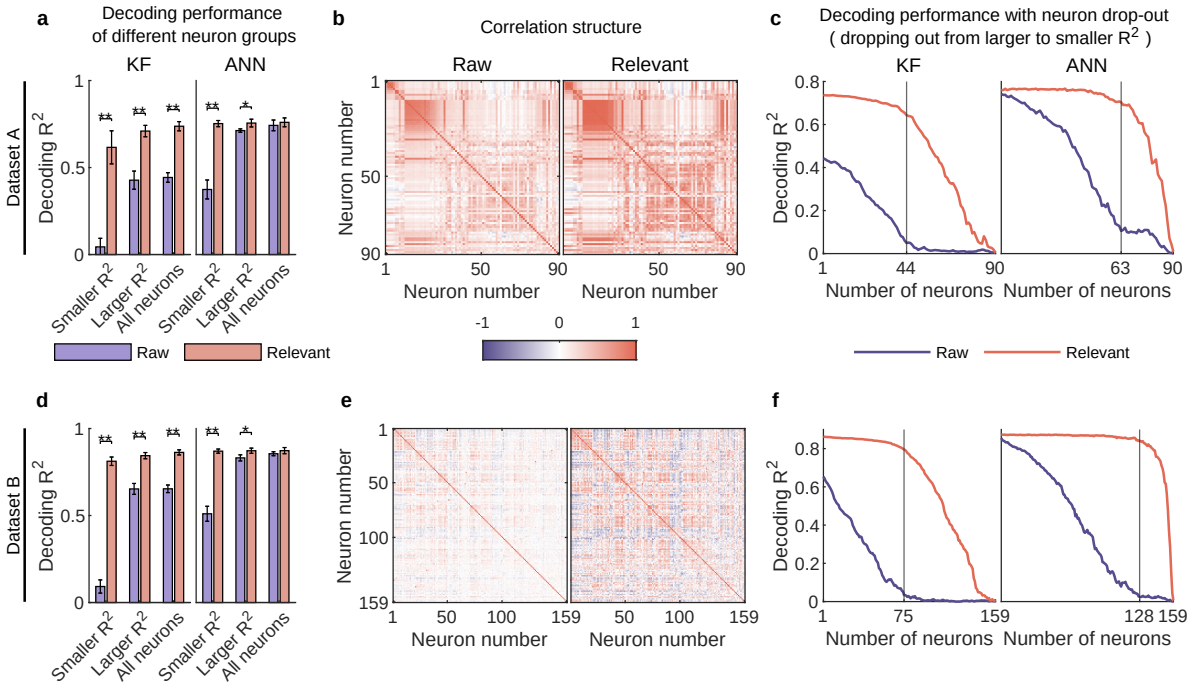

Figure 5: **Smaller** R^2 **neurons encode rich task information in complex nonlinear ways.** **a**, The comparison of decoding performance between raw (purple) and distilled signals (red) on dataset A with different neuron groups, including smaller R^2 neuron ($R^2 <= 0.03$), larger R^2 neuron ($R^2 > 0.03$), and all neurons. Error bars indicate mean ± s.d. across five cross-validation folds. Asterisks denote significance of Wilcoxon rank-sum test with $^{\star}P < 0.05$, $^{\star\star}P < 0.01$. **b**, The correlation matrix of all neurons of raw (left) and task-relevant (right) signals on dataset A. Neurons are ordered to highlight correlation structure (details in Methods). **c**, The decoding performance of KF (left) and ANN (right) with neurons dropped out from larger to smaller R^2 on dataset A. The vertical gray line indicates the number of dropped neurons at which raw and task-relevant signals have the greatest performance difference. **d-f**, Same as **a-c**, for dataset B.

overestimation of the neural dimensionality of task-relevant signals.

2.5. Distilled task-relevant signals uncover that smaller R^2 *neurons encode rich task information in complex nonlinear ways.*

The results presented in Section 2.3 regarding PDs demonstrate that irrelevant signals significantly impact smaller R^2 neurons and weakly impact larger R^2 neurons. Under the interference of irrelevant signals, it is difficult to explore the amount of task information in neuronal activity. Given that we have accurately separated the task-relevant and irrelevant signals, we explored whether irrelevant signals would mask some encoded information of neuronal activity, especially for smaller R^2 neurons.

To answer the question, we divided the neurons into two groups of smaller R^2

($R^2 <= 0.03$) and larger R^2 ($R^2 > 0.03$), and then used decoding models to assess how much information is encoded in raw and distilled signals. As shown in Fig. 5a, for the smaller R^2 neuron group, both KF and ANN decode task information poorly on raw signals, but achieve high decoding performance using relevant signals. Specifically, the KF decoder (left plot, Fig. 5a) improves the decoding R^2 significantly from 0.044 to 0.616 (improves by about 1300%; $P < 0.01$, Wilcoxon rank-sum test) after signal distillation; the ANN decoder (right plot, Fig. 5a) improves from 0.374 to 0.753 (improves by about 100%; $P < 0.01$, Wilcoxon rank-sum test). For the larger R^2 neuron group, the decoding performance of relevant signals with ANN does not improve much compared with the decoding performance of raw signals, but the decoding performance of relevant signals with KF is significantly better than that of raw signals ($P < 0.01$, Wilcoxon rank-sum test). Similar results are obtained with datasets B (Fig. 5d) and C (Supplementary Fig. S7d). These results indicate that irrelevant signals mask task information encoded by neuronal populations, especially for smaller R^2 neurons with a higher degree of nonlinearity, and that smaller R^2 neurons actually encode rich task information.

The fact that the smaller R^2 neurons encode rich information seems unexpected, and interestingly, we cannot obtain this rich information by just distilling smaller R^2 neurons. This leads to two alternative cases. The first is that the larger R^2 neurons leak their information to the smaller R^2 neurons, causing them contain too much task information. The second is that the smaller R^2 neurons per se contain a lot of information, and the larger R^2 neurons help the smaller R^2 neurons to restore their original appearance. We first tested the first case and found it does not hold for two reasons. Firstly, our model constrains distilled neuronal activity to be similar to the corresponding original neuronal activity (see Fig. 3i and Supplementary Fig. S2), inhibiting the generation of arbitrarily shaped neuronal activity, such as that of other neurons, so it is impossible for our model to add the activity of larger R^2 neurons to that of smaller R^2 neurons. To check this, we compared the neural similarity (R^2) of each distilled neuron to all raw neurons. We found 78/90 (87%, dataset A), 153/159 (96%, dataset B), 91/91 (100%, dataset C) distilled neurons are most similar to the corresponding neurons, and the other distilled neurons belong to the top four similar to the corresponding neurons, demonstrating the distilled neuronal activity is similar to the corresponding raw neuronal activity. Secondly, if this large amount of information is compensated by other neurons, the residuals should also contain an equally large amount of information, but they only contain a little information (Fig. 2c,g,k). Given these two reasons, the first case is rejected. Then we tested the second case. To verify the second case, we simulated a situation where the smaller R^2 neurons contain a certain amount of task information, but the task information cannot be decoded from these neurons due to being covered by noise (see Methods), to see if d-VAE can restore these neurons' original appearance. Results (Supplementary Fig. S8a-c) show that for smaller R^2 neurons, the decoding R^2 of distilled signals (0.362, 0.401 for KF and ANN) is significantly higher than that of raw signals (0.019, 0.063 for KF and ANN; $P < 0.01$, Wilcoxon rank-sum test), and is more closer to that of ground truth (0.454, 0.467 for KF and ANN). These

results approve the second case. Taken together, these results demonstrate that the smaller R^2 neurons indeed contain rich task information.

Given that both smaller and larger R^2 neurons encode rich task information, it is worth noting that the sum of the decoding performance of smaller R^2 neurons and larger R^2 neurons is significantly greater than that of all neurons for relevant signals (red bar, Fig. 5a,d and Supplementary Fig. S7a), demonstrating that movement parameters are encoded very redundantly in neuronal population. In contrast, we can not find this degree of neural redundancy in raw signals (purple bar, Fig. 5a,d and Supplementary Fig. S7a) because the encoded information of smaller R^2 neurons are masked by irrelevant signals. Therefore, these smaller R^2 neurons, which are usually ignored, are actually useful and play a critical role in supporting neural redundancy. Generally, cortical redundancy can arise from neuronal correlations, which are critical for revealing certain aspects of neural circuit organization [30]. Accordingly, we visualized the ordered correlation matrix of neurons (see Methods) for both raw and relevant signals (Fig. 5b,e and Supplementary Fig. S7b) and found that the neuronal correlation of relevant signals is stronger than that of raw signals. These results demonstrate that irrelevant signals weaken the neuronal correlation, which may hinder the accurate investigation of neural circuit organization.

Considering the rich redundancy and strong correlation of neuronal activity, we wondered whether the neuronal population could utilize redundant information from other neurons to exhibit robustness under the perturbation of neuronal destruction. To investigate this question, we evaluated the decoding performance of dropping out neurons from larger R^2 to smaller R^2 on raw and relevant signals. The results (Fig. 5c,f and Supplementary Fig. S7c) show that the decoding performance of the KF and ANN on raw signals (purple line) decreases steadily before the number of neurons marked (vertical gray line), and the remaining smaller R^2 neurons decode task information poorly. In contrast, even if many neurons are lost, the decoding performance of KF and ANN on relevant signals (red line) maintains high accuracy. This finding indicates that task-relevant signals are robust to the disturbance of neuron drop-out, and smaller R^2 neurons play a critical role in compensating for the failure of larger R^2 neurons. In contrast, this robustness can not be observed in raw signals because irrelevant signals mask neurons' information and weaken their correlation. Notably, the ANN outperforms the KF when only smaller R^2 neurons are left (Fig. 5c,f and Supplementary Fig. S7c), suggesting that smaller R^2 neurons can fully exploit their nonlinear ability to cope with large-scale neuronal destruction.

2.6. Distilled task-relevant signals uncover that signals composed of smaller variance PCs encode rich task information in complex nonlinear ways.

The results presented in Section 2.4 regarding subspace overlap show that irrelevant signals have a small impact on larger variance PCs but dominate smaller variance PCs. Therefore, we aimed to investigate whether irrelevant signals would mask some encoded

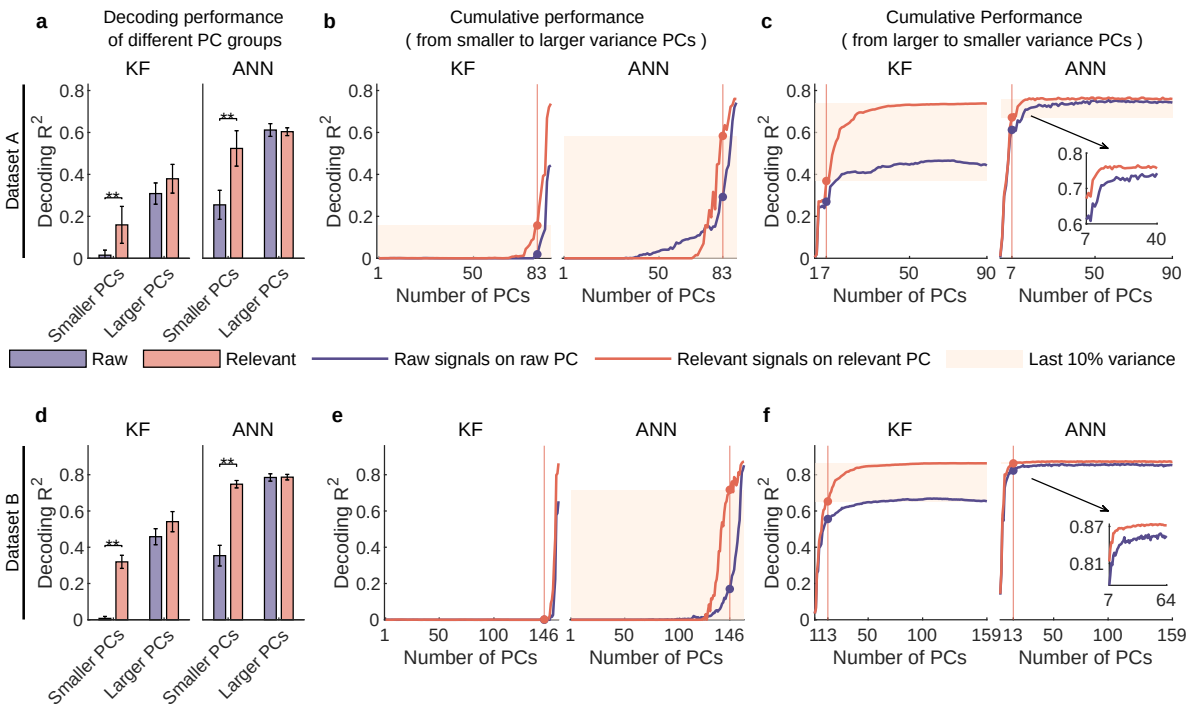

Figure 6: **Signals composed of smaller variance PCs encode rich task information in complex nonlinear ways.** **a**, The comparison of decoding performance between raw (purple) and distilled signals (red) composed of different raw PC groups, including smaller variance PCs (the proportion of irrelevant signals that make up raw PCs is higher than that of relevant signals), larger variance PCs (the proportion of irrelevant signals is lower than that of relevant ones) on dataset A. Error bars indicate mean ± s.d. across five cross-validation folds. Asterisks denote significance of Wilcoxon rank-sum test with $^{\star}P < 0.05$, $^{\star\star}P < 0.01$. **b**, The cumulative decoding performance of signals composed of cumulative PCs that are ordered from smaller to larger variance using KF (left) and ANN (right) on dataset A. The red patches indicate the decoding ability of the last 10% variance of relevant signals. **c**, The cumulative decoding performance of signals composed of cumulative PCs that are ordered from larger to smaller variance using KF (left) and ANN (right) on dataset A. The red patches indicate the decoding gain of the last 10% variance signals of relevant signals superimposing on their top 90% variance signals. The inset shows the partially enlarged plot for view clearly. **d-f**, Same as **a-c**, but for dataset B.

information of neural population, especially signals composed of smaller variance PCs.

To answer the question, we compared the decoding performance of raw and distilled signals with different raw PC groups. Specifically, we firstly divided the raw PCs into two groups, that is, smaller variance PCs and larger variance PCs, defined by ratio of relevant to irrelevant signals in the raw PCs (the red triangle, see Fig. 4c,g and Supplementary Fig. S3c). Then we projected raw and distilled signals onto these two PC groups and got the corresponding signals. Results show that, for the smaller

variance PC group, both KF and ANN achieve much better performance on distilled signals than raw signals ($P < 0.01$, Wilcoxon rank-sum test, for ANN), whereas for the larger variance PC group, the decoding performance of relevant signals does not improve a lot compared with the decoding performance of raw signals (see Fig. 6a,d and Supplementary Fig. S7a). These results demonstrate that irrelevant signals mask the task information encoded by different PC groups, especially for signals composed of smaller variance PCs (smaller variance PC signals), and smaller variance PC signals actually encode rich task information.

The above results are based on raw PCs. However, raw PCs are biased by irrelevant signals and thus cannot faithfully reflect the characteristics of relevant signals. As we have successfully separated the task-relevant signals, we aimed to explore how task information of distilled signals is distributed across relevant PCs. To do so, we used decoding models to evaluated the amount of task information contained in cumulative PCs of relevant signals (using raw signals as a comparison). The cumulative variance explained by PCs in descending and ascending order of variance and the dimensionality corresponding to the top 90% variance signals (called primary signals) and the last 10% variance signals (called secondary signals) are shown in Supplementary Fig. S6.

Here we first investigated secondary signals' decoding ability solely by accumulating PCs from smaller to larger variance. The results show that, for relevant signals, KF can hardly decode task information solely using secondary signals (red line; left plot, Fig. 6b,e and Supplementary Fig. S7e), but ANN can decode rich information (red line; right plot, Fig. 6b,e and Supplementary Fig. S7e). These results indicate that smaller variance PC signals encode rich information in complex nonlinear ways. In contrast, when using raw signals composed of the same number of dimensions as the secondary signals (purple line, Fig. 6b,e and Supplementary Fig. S7e), the amount of information identified by ANN is significantly smaller than that of relevant secondary signals ($P < 0.01$, Wilcoxon rank-sum test). These results demonstrate that irrelevant signals obscure these neural dimensions and make them seem insignificant, indicating that task information is distributed in a higher-dimensional subspace than expected from raw signals.

We then investigated the effect of superimposing secondary signals on primary signals by accumulating PCs from larger to lower variance. The results (Fig. 6c,f and Supplementary Fig. S7f) show that secondary signals improve the decoding performance of ANN a little but improve the decoding performance of KF a lot. The discrepancy between the two decoders reflects their different abilities to utilize the information within the signal. KF cannot use the nonlinear information in primary signals as effectively as ANN can and thus requires secondary signals to improve decoding performance. Notably, the improvement of KF using secondary signals is significantly higher than using raw signals composed of the same number of dimensions as the secondary signals ($P < 0.01$, Wilcoxon rank-sum test). These results demonstrate that irrelevant signals conceal the smaller variance PC signals, making their encoded information difficult to be linearly decoded, suggesting that task information exists in a higher-dimensional

subspace than anticipated from raw signals. Interestingly, we can find that although secondary signals nonlinearly encode task information and are decoded poorly by linear decoders, they considerably improve KF performance by superimposing on primary signals (Fig. 6c,f and Supplementary Fig. S7f left); and the sum of the sole decoding performance of primary and secondary signals is lower than the decoding performance of full signals. These results indicate that the combination of smaller and larger variance PCs produces a synergy effect [31] enabling secondary signals that cannot be linearly decoded to improve the linear decoding performance.

Finally, we explored which aspect of movement parameters was improved by superimposing the secondary signals on the primary ones with KF. In BMIs, directional control has achieved great success [8, 9], but precise speed control, especially at lower speeds such as hold or stop, has always been challenging [10, 11]. Thus we hypothesized that these signals might improve the lower-speed velocity. To test this, we divided samples into lower-speed and higher-speed regions and assessed which region improved the most by superimposing the secondary signals (see details in Methods). After superimposing the secondary signals, the absolute improvement ratio of the lower-speed region is significantly higher than that of the higher-speed region ($P < 0.05$, Wilcoxon rank-sum test; Supplementary Fig.S9a,b,c). Furthermore, we visualized the relative improvement ratio of five example trials for the two regions, and the results (Supplementary Fig. S9d) demonstrate that secondary signals significantly improve the estimation of lower speed. These findings indicate that the secondary signals enhance the lower-speed control and motivate further studies of these smaller variance PC signals.

2.7. Distilled task-relevant signals suggest that motor cortex may use a linear readout mechanism to generate movement behaviors.

Understanding the readout mechanism of the motor cortex is crucial for both neuroscience and neural engineering, which remains unclear. By filtering out the interference of task-irrelevant signals, we found a stunning result: the linear decoder KF achieves comparable performance to that of the nonlinear decoder ANN ($P = 0.10, 0.15$, and 0.55 for datasets A, B, and C, Wilcoxon rank-sum test; Fig. 2b,f,g). Considering the decoding performance and model complexity (the simplicity principle, also called Occam's razor), movement behaviors are more likely to be generated by the linear readout, suggesting linear readout is performed in the motor cortex.

However, one might doubt that it is our distillation model that makes signals which originally require nonlinear decoding linearly decodable. To address this concern, we conducted a simulation experiment where linear decoding is significantly inferior to nonlinear decoding to see if signals processed by our model could enable linear decoders to achieve performance similar to that of nonlinear decoders (see Methods). Results (Supplementary Fig. S8d-f) show that the difference of decoding R^2 between KF and ANN on distilled signals is 0.146, which is comparable to the difference (0.162) on raw signals ($P = 0.15$, Wilcoxon rank-sum test). This demonstrate that our model cannot

make linear decoders achieve similar performance as nonlinear decoders, thus eliminating the doubt.

In summary, these findings demonstrate that task-irrelevant signals significantly complicate the readout of task information and provide compelling evidence supporting the notion that the motor cortex uses a linear readout mechanism to generate movement behaviors.

3. Discussion

In this study, we proposed a new perspective for studying neural mechanisms, namely, using separated accurate task-relevant signals instead of raw signals; and we provided a novel distillation framework to define, extract, and validate task-relevant signals. By separating task-relevant and irrelevant signals, we found that neural responses previously considered trivial encode rich task information in complex nonlinear ways. Furthermore, we found that linear decoders can achieve comparable performance to that of nonlinear decoders, providing compelling evidence for the presence of linear readout in the motor cortex. Overall, our results reveal unexpected complex encoding but simple decoding mechanisms in the motor cortex.

3.1. Signal separation by d-VAE.

Task-relevant patterns can be extracted either at single-neuron or latent neural population levels. In our study, we focused on the single-neuron level, as this preserves the unique properties of individual neurons, while extracting at the population level would distort these properties. By maintaining the properties of each neuron, researchers can investigate how the neuronal population performs when one of the neurons is destroyed. This kind of analysis is particularly useful in closed-loop stimulation experiments that use electrophysiological [32] or optogenetic [33] interventions.

At the single-neuron level, it is common practice to use trial-averaged neuronal responses of the same task parameters to analyze neural mechanisms [28, 34]. However, trial averaging sacrifices single-trial information, thereby providing an incomplete characterization of neural activity. Furthermore, trial-averaged responses still contain a significant amount of task-irrelevant signals caused by uninstructed movements [35], which can lead to a contaminated version of task-relevant signals. In contrast, our model is capable of extracting clean task-relevant neural activity for every single trial. At the latent population level, existing latent variable models [20–23] focus on modeling some specific properties of latent population representations, such as linear or nonlinear dynamics [12, 20, 21], temporal smoothness [22], and interpretability [23]. Since these models make restrictive assumptions involving characterizing specific neural properties, they fail to capture other task-relevant signals that do not meet their assumptions, providing no guarantee that the generated signals preserve task information maximally. In contrast, our model aims to extract maximal task information at the single-neuron

level. To ensure this, we explicitly constrain the model to generate signals that maintain the neuronal properties while preserving task information to the greatest extent possible.

Although we made every effort, our model is still not able to perfectly extract task-relevant neural signals, resulting in a small amount of task information leakage in the residuals. Nevertheless, the signals distilled by our model are reliable, and the minor imperfections do not affect the conclusions drawn from our analysis. In the future, better models can be developed to extract task-relevant signals more accurately.

3.2. Implications for analyzing neural activity by separation.

Studying neural mechanisms through noisy signals is akin to looking at flowers in a fog, which is difficult to discern the truth. Thus, removing the interference of irrelevant signals is necessary and beneficial for analyzing neural activity, whether at the single-neuron level or population level.

At the single-neuron level, trial-to-trial neuronal variability poses a significant challenge to identifying the actual neuronal pattern changes. The variability can arise from various sources, including meaningless noise [6], meaningful but task-irrelevant neural processes [35], and intrinsic components of neural encoding [36]. However, it is still unclear to what extent each source contributes to the variability [6]. By separating task-relevant and irrelevant parts, we could roughly determine the extent to which these two parts contribute to the variability and explore which type of variability these two parts may contain. Our results demonstrate that task-irrelevant signals are a significant contributor to variability, which may include both meaningless noise and meaningful but task-irrelevant signals as task-irrelevant signals are not pure noise and may carry some structures (thick blue line, Fig. 4b,f and Supplementary Fig. S3b). Notably, task-relevant signals also exhibit some variability, which may arise from intrinsic components of neural encoding and provide the neural basis for motor learning [37]. Moreover, eliminating the variability caused by irrelevant signals enables us to better observe and compare actual neuronal pattern changes and may facilitate the study of learning mechanisms [38, 39].

At the population level, determining the neural dimensionality of specific tasks from raw signals is challenging since it is difficult to discern how many variances correspond to irrelevant signals, which often depend heavily on signal quality. A previous study [40] demonstrated, through simulation experiments involving different levels of noise, that such noise makes methods overestimate the neural dimensionality of tasks. Our results, consistent with theirs, indicate that task-irrelevant signals can cause an overestimation of the neural dimensionality of task-relevant responses (Supplementary Fig. S6). These findings highlight the need to filter out irrelevant signals when estimating the neural dimensionality. It is important to note that the dimensionality of neural subspaces encoding task information cannot be accurately determined by the variance they capture. Estimating the dimensionality accurately requires considering the amount of task information encoded by signals distributed within these subspaces.

This is because the variance of neural signals does not directly reflect the amount of task information they encode. For example, task-irrelevant signals occupy some neural subspaces without containing task information. Furthermore, this perspective of signal separation has broader implications for other studies. For instance, researchers can isolate neural signals corresponding to different tasks and explore their shared and exclusive patterns to uncover underlying common and unique mechanisms of different behaviors [13].

3.3. Implications for exploring neural mechanisms by separation

At the single-neuron level, previous studies [31, 41] have shown that neuronal ensembles redundantly encode movement behaviors in the motor cortex. However, our results reveal a significantly higher level of redundancy than previously reported. Specifically, prior studies found that the decoding performance steadily declines as neurons drop out, which is consistent with our results drawn from raw signals. In contrast, our results show that decoders maintain high performance on distilled signals even when many neurons drop out. Our findings reinforce the idea that movement behavior is redundantly encoded in the motor cortex and demonstrate that the brain is robust enough to tolerate large-scale neuronal destruction while maintaining brain function [42].

At the population level, previous studies have proposed that motor control is achieved through low-dimensional neural manifolds [15, 43]. However, our results challenge this idea by showing that signals composed of smaller variance PCs nonlinearly encode a significant amount of task information. This suggests that task information is distributed in a higher-dimensional neural space than previously thought. Interestingly, although smaller variance PC signals nonlinearly encode task information, their task information can be linearly decoded by superimposing them onto larger variance PC signals. This result is consistent with the finding that nonlinear mixed selectivity can yield high dimensional neural responses and thus allow linear readout of task information by downstream neurons [3, 4]. Moreover, we found that smaller variance PC signals can improve precise motor control, such as lower speed control. Analogously, recent studies have found that smaller variance PCs of hand postures are task-dependent and relate to the precise and complex postures [44]. These findings suggest that neural signals with lower variance PCs are relevant to precise movement control, highlighting their importance in motor control.

In the motor cortex, in what form downstream neurons read out task information is still an open question. By filtering out task-irrelevant signals, our study found that accurate decoding performance can be achieved through linear readout, suggesting that the motor cortex may perform linear readout to generate movement behaviors. Similar findings have been reported in other cortices, such as the inferotemporal cortex (IT) [45], perirhinal cortex (PRH) [46], and somatosensory cortex [25], supporting the idea of linear readout as a general principle in the brain. However, further experiments are needed to verify this hypothesis across a wider range of cortical regions. While

neurons encode significant task information nonlinearly, our study demonstrates that when neuronal assemblies with diverse firing patterns collaborate to decode information, they do not necessarily need to fully exert their nonlinear ability. Instead, a simple linear combination of these assemblies can accomplish the decoding task. This finding suggests that the complexity of encoding mechanisms underlies the simplicity of decoding mechanisms.

With regard to studying decoding mechanisms, recent studies [16, 17] have focused on investigating how the brain decodes task information in the presence of noise. Unlike their works, we focus on studying the decoding mechanism after removing the noise (irrelevant signals). Although our research perspectives differ, our results support their idea that the brain needs nonlinear operations to suppress noise interference [17]. However, in principle, denoising (or filtering out task-irrelevant signals) and decoding are two separate steps. Using a communication system as a metaphor, the receiver should first denoise the signal received from the sender and then decrypt the message. The same should be true for the brain. Therefore, removing irrelevant signals to study the readout mechanism is reasonable. Additionally, investigating how the brain filters out noise or separates task-irrelevant factors is a promising research direction [47]. Distilled task-relevant signals can serve as reliable reference signals to facilitate this study. Furthermore, our study reveals that irrelevant signals are the most critical factor affecting accurate and robust decoding, and achieving accurate and robust linear decoding requires weak neural responses. These findings have two important implications for developing accurate and robust BMIs: designing preprocessing filtering algorithms or developing decoding algorithms that include filtering out task-irrelevant signals, and paying attention to the role of weak neural responses in motor control. More generally, our study provides a powerful framework for separating task-relevant and irrelevant signals, which can be applied to other cortical data to uncover more hidden neural mechanisms.

4. Methods

4.1. Dataset and preprocessing

Three datasets with different paradigms are employed, including obstacle avoidance task dataset [48], center-out reaching task dataset [49], and self-paced reaching task dataset [50].

The first dataset is the obstacle avoidance dataset. An adult male Rhesus monkey was trained to use the joystick to move the computer cursor to bypass the obstacle and reach the target. Neural data were recorded from the monkey's upper limb area of the dorsal premotor (PMd) using a 96-electrode Utah array (Blackrock Microsystems Inc., USA). Multi-unit activity (MUA) signals are used in the present study. The corresponding behavioral data (velocity) were simultaneously collected. There are two days of data (20140106 and 20140107), and each day contains 171 trials on average. All

animal handling procedures were authorized by the Animal Care Committee at Zhejiang University, China, and conducted following the Guide for Care and Use of Laboratory Animals (China Ministry of Health).

The second dataset is publicly available and provided by Kording Lab [49]. The monkey was trained to complete two-dimensional 8-direction center-out reaching tasks. We used two days of data from subject C (20161007 and 20161011). Each day contains 190 trials on average. Neural data are spike-sorted PMd signals. The behavioral data were simultaneously collected in instantaneous velocity.

The third dataset is publicly available and provided by Sabes Lab (Zenodo dataset) [50]. An adult male Rhesus monkey was trained to finish self-paced reaching tasks within an 8-by-8 square grid. There are no inter-trial intervals during the experiment. Neural data were recorded from the monkey's primary motor cortex (M1) area with a 96-channel silicon microelectrode array. The neural data are the multi-unit activity (MUA) signals. Hand velocity was obtained from the position through a discrete derivative. The recording period for the data (20170124 01) is about 10 minutes.

For all datasets, the neural signals were binned by a 100ms sliding window without overlap. As a preprocess, we smoothed the neural signals using a moving average filter with three bins. We excluded some electrode activities with low mean firing rates (<0.5 Hz mean firing rates across all bins) and did not perform any other pre-selection to select neurons. For the computation of the Fano factor, we chose twelve and fourteen points as the thresholds of trial length for datasets A and B, respectively; trials with a length less than the threshold were discarded (discard about 7% and 2% trials for datasets A and B), trials longer than the threshold were truncated to threshold length from the starting point. Since dataset C has no trial information, FF is not calculated for this dataset. For the analysis of datasets A and B, we selected one day of these two datasets for analysis (20140107 for dataset A and 20161011 for dataset B).

4.2. Simulation experiments

In this experiment, we simulated four neurons, including two larger R^2 neurons (greater than 0.4) and two smaller R^2 neurons (lower than 0.03). The larger R^2 neurons are strongly tuned neurons and are added with small Gaussian noise. In contrast, the smaller R^2 neurons strongly nonlinearly encode task information and are added with large Gaussian noise. We regarded the signals without adding Gaussian noise as ground-truth signals and those with Gaussian signals as raw signals. We used the velocity of dataset B (20161011) for simulation. The simulation dataset A includes the four neurons, which simulates the situation where the smaller R^2 neurons contain a lot of task information, but the task information cannot be decoded from these neurons due to being covered by noise. The simulation dataset B includes the two larger R^2 neurons, which simulates the situation where linear decoding is significantly inferior to nonlinear decoding.

The encoding model of larger R^2 neurons is as follows:

$$x_i(t) = b + m \mid \mathbf{v}(t) \mid \cos(\theta(t) - \theta_{PDi}) + b_s \mid \mathbf{v}(t) \mid + \epsilon_i(t), \tag{1}$$

where the subscript i refers to the ith unit of N neurons, $N = 2$ in this experiment, t represents time, $b = 30$ Hz represents the baseline firing rate of neurons, $m = 0.25$ Hz per cm s^{-1} indicates the modulation depth, the PDs of neurons θ_{PDi} (i=1, 2) are set to 30° and 60°, $\epsilon_i(t) = \mathcal{N}(0, 0.3)$ denotes random Gaussian noise where the mean is zero and the standard deviation is 0.3, $\mathbf{v}$ represents velocity, $\mid \mathbf{v} \mid$ represents the norm of velocity (speed), $b_s = 0.25$ Hz per cm s^{-1} denotes speed bias.

The encoding model of smaller R^2 neurons is as follows:

$$x_i(t) = b + m \mid \mathbf{v}(t) \mid \cos(\theta(t) - \theta_{PDi}) + b_s \mid \mathbf{v}(t) \mid + b_{ss} \mid \mathbf{v}(t) \mid^2 + \epsilon_i(t), \tag{2}$$

where $b = 30$ Hz, $m = 0.25$ Hz per cm s^{-1}, the PDs of neurons θ_{PDi} (i=1, 2) are set to 40° and 50°, $\epsilon_i(t) = \mathcal{N}(0, 1)$ denotes random Gaussian noise where the mean is zero and the standard deviation is one, $b_s = 0.25$ Hz per cm s^{-1}, $b_{ss} = 0.1$ Hz per cm^2 s^{-1} denotes the bias of speed square for increasing the encoding nonlinearty of neurons.

4.3. Variational autoencoders

Variational autoencoders (VAEs) [26] are famous latent variable generative models and can use latent representations $\mathbf{z} \sim p(\mathbf{z})$ to generate data $\mathbf{x}$ by conditional distribution $p_\theta(\mathbf{x} \mid \mathbf{z})$, that is, $p_\theta(\mathbf{x}) = \int_{\mathbf{z}} p(\mathbf{z}) p_\theta(\mathbf{x} \mid \mathbf{z}) \mathrm{d}\mathbf{z}$. The usual training objective is maximum marginal likelihood $\log p_\theta(\mathbf{x})$. Since directly computing the integration is intractable, VAE propose an amortized inference distribution $q_\phi(\mathbf{z} \mid \mathbf{x})$ and jointly optimize the evidence lower bound (ELBO) to the log-likelihood:

$$\mathcal{L}_{ELBO}(\mathbf{x}) = \mathbb{E}_{\mathbf{z} \sim q_\phi(\mathbf{z}|\mathbf{x})} \left[p_\theta(\mathbf{x} \mid \mathbf{z}) \right] - D_{KL}(q_\phi(\mathbf{z} \mid \mathbf{x}) \| p(\mathbf{z})) \leq \log p_\theta(\mathbf{x}), \tag{3}$$

where the first term of right hand side of Eq. (3) is called reconstruction term, the second term is called regularization term, $q_\phi(\mathbf{z} \mid \mathbf{x})$ is usually parameterized with a neural network called encoder or inference model with parameters ϕ, and $p_\theta(\mathbf{x} \mid \mathbf{z})$ is also parameterized with a neural network called decoder or generative model with parameters θ. $p(\mathbf{z})$ is the prior over the latent representations and is set to be Gaussian distribution $\mathcal{N}(\mathbf{0}, \mathbf{I})$ in vallina VAE, D_{KL} denotes the Kullback-Leibler divergence.

4.4. Distill-VAE (d-VAE)

Notations. $\mathbf{x} \in \mathbb{R}^n$ denotes raw neural signals. $\mathbf{x}_r \in \mathbb{R}^n$ represents task-relevant signals. $\mathbf{x}_i = \mathbf{x} - \mathbf{x}_r \in \mathbb{R}^n$ represents task-irrelevant signals. $\mathbf{z} \in \mathbb{R}^d$ denotes the latent neural representations. $\mathbf{y} \in \mathbb{R}^k$ represents kinematics. $f : \mathbb{R}^n \to \mathbb{R}^d$ represents the inference model (encoder) of VAE. $g : \mathbb{R}^d \to \mathbb{R}^n$ represents the generative model (decoder) of VAE.

To distill task-relevant neural signals, our approach utilizes the trade-off between the decoding and generating abilities of distilled task-relevant signals $\mathbf{x}_r$. The basic assumption is generated task-relevant signals that contain task-irrelevant signals harms decoding ability. Our method for distilling task-relevant signals consists of three steps, including identifying latent representations $\mathbf{z}$, generating task-relevant signals $\mathbf{x}_r$, and decoding task-relevant signals $\mathbf{x}_r$.

4.4.1. Identfiying latent representations $\mathbf{z}$ Identifying latent representations containing task-relevant information is the crucial part because latent representations influences the subsequent generation. Effective representations are more likely to generate proper task-relevant neural signals $\mathbf{x}_r$. d-VAE identifies latent representations with inference model f, that is, $\mathbf{z} = f(\mathbf{x})$, and guides latent representations containing task-information through an affine map $h : \mathbb{R}^d \to \mathbb{R}^k$ under the loss $\mathcal{L}_{dec1}$,

$$\mathcal{L}_{dec1} = \mathrm{MSE}(h(\mathbf{z}), \mathbf{y}), \tag{4}$$

where $\mathrm{MSE}(\cdot, \cdot)$ denotes mean squared loss. In other words, we encourage latent representations to decode kinematics to distill task-relevant information.

4.4.2. Generating task-relevant signals $\mathbf{x}_r$ After identifying latent representations $\mathbf{z}$, we send latent representations to the generative model g to generate task-relevant neural signals $\mathbf{x}_r$, that is, $\mathbf{x}_r = g(\mathbf{z})$. We use following loss to make task-relevant signals reconstruct raw signals as much as possible:

$$\mathcal{L}_{rec} = \mathrm{Poisson}(\mathbf{x}_r, \mathbf{x}), \tag{5}$$

where $\mathrm{Poisson}(\cdot, \cdot)$ denotes Poisson negative log likelihood loss. It is important to note that optimizing the generation of task-relevant signals to accurately reconstruct noisy raw signals may result in the inclusion of many task-irrelevant signals in the generated signals, which deviates from our initial goal of extracting task-relevant signals. In the following subsection, we will introduce how to avoid generating task-irrelevant signals.

4.4.3. Decoding task-relevant signals $\mathbf{x}_r$ As mentioned above, if the generation of task-relevant signals $\mathbf{x}_r$ is only guided by $\mathcal{L}_{rec}$, generated signals may contain more task-irrelevant signals. To avoid generated signals containing task-irrelevant signals, we introduce decoding loss $\mathcal{L}_{dec2}$ to constrain $\mathbf{x}_r$ to decode task information. The basic assumption is that task-irrelevant signals act like noise for decoding task information and are detrimental to decoding. Thus, there is a trade-off between generating and decoding ability of $\mathbf{x}_r$: the more task-irrelevant signals $\mathbf{x}_r$ contains, the more decoding performance $\mathbf{x}_r$ loses. The decoding loss $\mathcal{L}_{dec2}$ is as follows:

$$\mathcal{L}_{dec2} = \mathrm{MSE}(h(f(\mathbf{x}_r)), \mathbf{y}). \tag{6}$$

We use the same networks f and h for $\mathbf{x}_r$ and $\mathbf{x}$ in our experiment, because $\mathbf{x}_r$ can act as data augmentation and make f distill robust representations without increasing model parameters. In addition, we combine the two decoding loss as one loss:

$$\mathcal{L}_{dec} = \frac{1}{2}(\mathcal{L}_{dec1} + \mathcal{L}_{dec2}). \tag{7}$$

4.4.4. Learning the prior distribution with task information The prior distribution of latent representation is crucial because inappropriate prior assumptions can degrade latent representations and generated neural signals. Vanilla VAE uses a Gaussian prior $\mathcal{N}(\mathbf{0}, \mathbf{I})$ to regularize the space of latent representation $\mathbf{z}$. However, in neuroscience, the distribution of latent representations is unknown and may exceed the scope of Gaussian. Therefore we adopt neural networks $m : \mathbb{R}^k \to \mathbb{R}^d$ to learn the prior representation $\mathbf{z}_{prior}$ with kinematics $\mathbf{y}$, that is, $\mathbf{z}_{prior} = m(\mathbf{y})$. The prior representation $\mathbf{z}_{prior}$ and $\mathbf{z}$ are aligned by the Kullback–Leibler divergence:

$$\mathcal{L}_{KL} = D_{KL}(\mathbf{z} \| \mathbf{z}_{prior}). \tag{8}$$

Since $\mathbf{z}_{prior}$ and $\mathbf{z}$ are aligned and the generative network g models the relationship between $\mathbf{z}$ and $\mathbf{x}_r$, this is equivalent to indirectly establishing a neural encoding model from $\mathbf{y}$ to $\mathbf{x}_r$. Thus, we can observe the change of $\mathbf{z}_{prior}$ and $\mathbf{x}_r$ by changing $\mathbf{y}$ and can better understand the encoding mechanism of neural signals.

4.4.5. End-to-end optimization d-VAE is optimized in an end-to-end manner under the following loss:

$$\mathcal{L} = \mathcal{L}_{rec} + \beta \mathcal{L}_{KL} + \alpha \mathcal{L}_{dec}, \tag{9}$$

where β and α are hyperparameters, β is used to adjust the weight of KL divergence, and α determines the trade-off between reconstruction loss $\mathcal{L}_{rec}$ and decoding loss $\mathcal{L}_{dec}$.

In the training stage, we feed raw neural signals into the inference network f to get latent representation $\mathbf{z}$, which is regularized by $\mathbf{z}_{prior}$ coming from kinematics $\mathbf{y}$ and network m. Then we use $\mathbf{z}$ to decode kinematics $\mathbf{y}$ by affine layer h and send $\mathbf{z}$ to the generative networks g to generate neural signals $\mathbf{x}_r$. To ensure that $\mathbf{x}_r$ preserves decoding ability, we send $\mathbf{x}_r$ to f and h to decode $\mathbf{y}$. The whole model is trained in an end-to-end manner under the guidance of total loss. Once the model has been trained, we can feed raw neural signals to it to obtain task-relevant neural signals $\mathbf{x}_r$, and we can aslo generate task-relevant neural signals using the prior distribution $\mathbf{z}_{prior}$.

4.5. Cross-validation evaluation of models.

For each model, we use the five-fold cross-validation manner to assess performance. Specifically, we divide the data into five equal folds. In each experiment, we take one fold for testing and use the rest for training (taking three folds as the training set and one as the validation set). The reported performance is averaged over test sets of five experiments. The validation sets are used to choose hyperparameters. To avoid

overfitting, we apply the early stopping strategy. Specifically, we assess the criteria (loss for training distillation methods, R^2 for training ANN and KF) on the validation set every epoch in the training process. The model is saved when the model achieves better validation performance than the earlier epochs. If the model cannot increase by 1% of the best performance previously obtained within specified epochs, we stop the training process.

4.6. The strategy for selecting effective task-relevant signals.

As previously mentioned, the hyperparameter α plays a crucial role in balancing the trade-off between reconstruction and decoding loss. Once the appropriate value of α is determined, we can use this value to obtain accurate task-relevant signals for subsequent analysis. To determine the optimal value of α, we first enumerated different values of α to guide d-VAE in distilling the task-relevant signals. Next, we used ANN to evaluate the decoding R^2 of task-relevant (D_{re}) and irrelevant (D_{ir}) signals generated by each α value. Finally, we selected the α value with the criteria formula $0.75 \times D_{re} + 0.25 \times (1 - D_{ir})$. The α value that obtained the highest criteria score on the validation set was selected as the optimal value.

Note that we did not use neural similarity between task-relevant and raw signals as a criterion for selecting task-relevant signals. This is because determining the threshold for neural similarity is challenging. However, not using similarity as a criterion does not affect the selection of suitable signals because the decoding performance of task-irrelevant signals can indirectly reflect the degree of similarity between the generated task-relevant signals and the raw signals. Specifically, if the generated task-relevant signals are dissimilar to the raw signals, the task-irrelevant signals will contain many useful signals. In other words, when the neural similarity between task-relevant and raw signals is low, the decoding performance of task-irrelevant signals is high. Therefore, the decoding performance of irrelevant signals is a reasonable alternative to the neural similarity.

4.7. Implementation details for methods

All the VAE-based models use the Poisson observation function. The details of different methods are demonstrated as follows:

- d-VAE. The encoder of d-VAE uses two hidden layer multilayer perceptron (MLP) with 300 and 100 hidden units. The decoder of d-VAE is symmetric with the encoder. The dimension of the latent variable is set to 50. The prior networks use one hidden layer MLP with 300 units. The β is set to 0.001. The α is set to 0.3, 0.4, 0.7 for dataset A, B, and C, respectively.
- pi-VAE. The original paper obtains the approximate posterior of the latent variable using the label information (Eq.6 in the original paper), so the label information is used in the test stage. However, it is unreasonable to use label information

(kinematics) to extract task-relevant signals in the test stage, so we changed the model to not use label information to approximate the posterior. The parameters of the encoder, decoder and prior networks of pi-VAE are the same as d-VAE.

- VAE. The parameters of the encoder and decoder of VAE are the same as d-VAE.
- LFADS. The hidden units of the encoder for the generator's initial conditions, the controller, the generator are set to 200. The dimensionality of latent factor is set to 50. The dimensionality of inferred inputs is set to 1. The training strategy follows the practice of the original paper.
- PSID. The horizon parameter of PSID is set to 3, and the dimensionality of latent variable is set to 6.
- ANN. ANN has two hidden layers with 300 and 100 hidden units.
- KF. The matrix parameters of observation and state transition process are optimized with the least square algorithm.

4.8. Percentage of explained variance captured in a subspace.

We applied PCA to task-relevant and irrelevant signals to get relevant PCs and irrelevant PCs. Then we used the percentage variance captured (also called alignment index) to quantify how many variances of irrelevant signals can be captured by relevant PCs by projecting irrelevant signals onto the subspace composed of some relevant PCs and vice versa. The percentage of variance captured is:

$$A = \frac{\mathrm{Tr}\left(\mathbf{D}^{\mathrm{T}}\mathbf{C}\mathbf{D}\right)}{\mathrm{Tr}\left(\mathbf{C}\right)} \times 100\%, \tag{10}$$

where $\mathbf{D} \in \mathbb{R}^{N\times d}$ is a d-dimensional population basis over N neurons, $\mathbf{C} \in \mathbb{R}^{N\times N}$ is the covariance matrix of the neural signals, and $\mathrm{Tr}\left(\mathbf{C}\right) = \sum_{i=1}^{N} \lambda_i$, where λ_i is the ith largest eigenvalue for $\mathbf{C}$. The matrices $\mathbf{D}$ and $\mathbf{C}$ can be computed for both task-irrelevant and relevant signals. The percentage variance is a quantity between 0% and 100%.

4.9. The composition of raw signals' variance.

Suppose $\mathbf{x} \in \mathbb{R}^{1\times T}$, $\mathbf{y} \in \mathbb{R}^{1\times T}$, and $\mathbf{z} \in \mathbb{R}^{1\times T}$ are the random variables for a single neuron of task-relevant signals, task-irrelevant, and raw signals, where $\mathbf{z} = \mathbf{x} + \mathbf{y}$, T denotes the number of samples. The composition of raw signals' variance is as follows:

$$\begin{aligned}\mathrm{Var}(\mathbf{z}) &= \mathrm{Var}(\mathbf{x}+\mathbf{y}) = \mathbb{E}\left\{[\mathbf{x}-\mathbb{E}(\mathbf{x})] + [\mathbf{y}-\mathbb{E}(\mathbf{y})]\right\}^2 \\ &= \mathbb{E}[\mathbf{x}-\mathbb{E}(\mathbf{x})]^2 + \mathbb{E}[\mathbf{y}-\mathbb{E}(\mathbf{y})]^2 + 2\mathbb{E}[\mathbf{x}-\mathbb{E}(\mathbf{x})][\mathbf{y}-\mathbb{E}(\mathbf{y})] \\ &= \mathrm{Var}(\mathbf{x}) + \mathrm{Var}(\mathbf{y}) + 2\mathrm{Cov}(\mathbf{x},\mathbf{y}),\end{aligned} \tag{11}$$

where $\mathbb{E}$, Var, and Cov denote expectation, variance, and covariance, respectively. Thus, the variance of raw signals is composed by the variance of relevant signals $\mathrm{Var}(\mathbf{x})$, the variance of irrelevant signals $\mathrm{Var}(\mathbf{y})$, and the correlation between relevant and irrelevant signals $2\mathrm{Cov}(\mathbf{x},\mathbf{y})$. If there are N neurons, calculate the composition of each neuron separately and then add it up to get the total composition of raw signals.

4.10. Reordered correlation matrix of neurons.

The correlation matrix is reordered with a simple group method. The order of reordered neurons is determined from raw neural signals, which is then used for task-relevant signals.

The steps of the group method are as follows:

Step 1: We get the correlation matrix in original neuron order and set a list A that contains all neuron numbers and an empty list B.

Step 2: We select the neuron with the row number of the largest value of the correlation matrix except for the diagonal line and choose nine neurons in list A that are most similar to the selected neuron.

Step 3: Remove these selected neurons from list A, and add these selected neurons in descending order of correlation value in list B.

Step 4: Repeat steps 2 and 3 until list A is empty.

4.11. The improvement ratio of lower and higher speed regions

4.11.1. Split lower and higher speed regions Since the speed ranges of different datasets are different, it is hard to determine a common speed threshold to split lower and higher speed regions. Here we used the squared error as a criterion to split the two speed regions. And for the convenience of calculating the absolute improvement ratio, we need a unified benchmark for comparison. Therefore, we use half of the total squared error as the threshold. Specifically, first, we calculated all samples' total squared error (E_p) between actual velocity and predicted velocity obtained by primary signals only. Then we enumerated the speed from 1 to 50 with a step of 0.1 and calculated the total squared error of selected samples whose speed is less than the enumerated speed. Once the total squared error of selected samples is greater than or equal to the half total squared error of all samples ($0.5E_p$), the enumerated speed is set as the speed threshold. The samples whose speed is less than or equal to the speed threshold belong to lower speed regions, and those whose speed is greater than the speed threshold belong to higher speed regions. The squared error of the lower speed part (E_p^{low}) is approximately equal to that of the higher one E_p^{high}, that is, $E_p^{low} \approx E_p^{high} \approx 0.5E_p$ (the difference is negligible).

4.11.2. The absolute improvement ratio After splitting the speed regions, we calculated the improvement of the two regions by superimposing secondary signals to primary signals, and got the squared error of lower E_{p+s}^{low} and higher E_{p+s}^{high} regions. Then we calculated the absolute improvement ratio (AIR):

$$AIR_{low} = -\frac{E_{p+s}^{low} - E_p^{low}}{E_p^{low}} \approx -\frac{E_{p+s}^{low} - 0.5E_p}{0.5E_p} \tag{12}$$

$$AIR_{high} = -\frac{E_{p+s}^{high} - E_p^{high}}{E_p^{high}} \approx -\frac{E_{p+s}^{high} - 0.5E_p}{0.5E_p} \tag{13}$$

Since the two regions refer to a common standard ($0.5E_p$), the improvement ratio of the two regions can be directly compared, and that's why we call it the absolute improvement ratio.

4.11.3. The relative improvement ratio The relative improvement ratio (RIR) measures the improvement ratio of each sample relative to itself before and after superimposing secondary signals. The relative improvement ratio is computed as follows:

$$RIR^i = -\frac{E^i_{p+s} - E^i_p}{E^i_p}, \tag{14}$$

where i denotes the ith sample.

Data availability

The datasets are available for research purposes from the corresponding author on reasonable request.

Code availability

The code will be publically available in github (see https://github.com/eric0li/d-VAE).

Reference

[1] Nikolaus Kriegeskorte and Pamela K Douglas. Interpreting encoding and decoding models. *Current opinion in neurobiology*, 55:167–179, 2019.

[2] Shreya Saxena and John P Cunningham. Towards the neural population doctrine. *Current opinion in neurobiology*, 55:103–111, 2019.

[3] Stefano Fusi, Earl K Miller, and Mattia Rigotti. Why neurons mix: high dimensionality for higher cognition. *Current opinion in neurobiology*, 37:66–74, 2016.

[4] Mattia Rigotti, Omri Barak, Melissa R Warden, Xiao-Jing Wang, Nathaniel D Daw, Earl K Miller, and Stefano Fusi. The importance of mixed selectivity in complex cognitive tasks. *Nature*, 497(7451):585–590, 2013.

[5] Rony Azouz and Charles M Gray. Cellular mechanisms contributing to response variability of cortical neurons in vivo. *Journal of Neuroscience*, 19(6):2209–2223, 1999.

[6] A Aldo Faisal, Luc PJ Selen, and Daniel M Wolpert. Noise in the nervous system. *Nature reviews neuroscience*, 9(4):292–303, 2008.

[7] Rubén Moreno-Bote, Jeffrey Beck, Ingmar Kanitscheider, Xaq Pitkow, Peter Latham, and Alexandre Pouget. Information-limiting correlations. *Nature neuroscience*, 17(10):1410–1417, 2014.

[8] Apostolos P Georgopoulos, Andrew B Schwartz, and Ronald E Kettner. Neuronal population coding of movement direction. *Science*, 233(4771):1416–1419, 1986.

[9] Leigh R Hochberg, Daniel Bacher, Beata Jarosiewicz, Nicolas Y Masse, John D Simeral, Joern Vogel, Sami Haddadin, Jie Liu, Sydney S Cash, Patrick Van Der Smagt, et al. Reach and grasp by people with tetraplegia using a neurally controlled robotic arm. *Nature*, 485(7398):372–375, 2012.

[10] B Wodlinger, JE Downey, EC Tyler-Kabara, AB Schwartz, ML Boninger, and JL Collinger. Ten-dimensional anthropomorphic arm control in a human brain- machine interface: difficulties, solutions, and limitations. *Journal of neural engineering*, 12(1):016011, 2014.

[11] Yoh Inoue, Hongwei Mao, Steven B Suway, Josue Orellana, and Andrew B Schwartz. Decoding arm speed during reaching. *Nature communications*, 9(1):1–14, 2018.

[12] Mark M Churchland, John P Cunningham, Matthew T Kaufman, Justin D Foster, Paul Nuyujukian, Stephen I Ryu, and Krishna V Shenoy. Neural population dynamics during reaching. *Nature*, 487(7405):51–56, 2012.

[13] Juan A Gallego, Matthew G Perich, Stephanie N Naufel, Christian Ethier, Sara A Solla, and Lee E Miller. Cortical population activity within a preserved neural manifold underlies multiple motor behaviors. *Nature communications*, 9(1):1–13, 2018.

[14] Juan A Gallego, Matthew G Perich, Raeed H Chowdhury, Sara A Solla, and Lee E Miller. Long-term stability of cortical population dynamics underlying consistent behavior. *Nature neuroscience*, 23(2):260–270, 2020.

[15] John P Cunningham and Byron M Yu. Dimensionality reduction for large-scale neural recordings. *Nature neuroscience*, 17(11):1500–1509, 2014.

[16] Xaq Pitkow, Sheng Liu, Dora E Angelaki, Gregory C DeAngelis, and Alexandre Pouget. How can single sensory neurons predict behavior? *Neuron*, 87(2):411–423, 2015.

[17] Qianli Yang, Edgar Walker, R James Cotton, Andreas S Tolias, and Xaq Pitkow. Revealing nonlinear neural decoding by analyzing choices. *Nature communications*, 12(1):1–13, 2021.

[18] Joshua I Glaser, Ari S Benjamin, Raeed H Chowdhury, Matthew G Perich, Lee E Miller, and Konrad P Kording. Machine learning for neural decoding. *Eneuro*, 7(4), 2020.

[19] Matthew S Willsey, Samuel R Nason-Tomaszewski, Scott R Ensel, Hisham Temmar, Matthew J Mender, Joseph T Costello, Parag G Patil, and Cynthia A Chestek. Real-time brain-machine interface in non-human primates achieves high-velocity prosthetic finger movements using a shallow feedforward neural network decoder. *Nature Communications*, 13(1):1–14, 2022.

[20] Omid G Sani, Hamidreza Abbaspourazad, Yan T Wong, Bijan Pesaran, and Maryam M Shanechi. Modeling behaviorally relevant neural dynamics enabled by preferential subspace identification. *Nature Neuroscience*, 24(1):140–149, 2021.

[21] Chethan Pandarinath, Daniel J O'Shea, Jasmine Collins, Rafal Jozefowicz, Sergey D Stavisky, Jonathan C Kao, Eric M Trautmann, Matthew T Kaufman, Stephen I Ryu, Leigh R Hochberg, et al. Inferring single-trial neural population dynamics using sequential auto-encoders. *Nature methods*, 15(10):805–815, 2018.

[22] Byron M Yu, John P Cunningham, Gopal Santhanam, Stephen Ryu, Krishna V Shenoy, and Maneesh Sahani. Gaussian-process factor analysis for low-dimensional single-trial analysis of neural population activity. *Advances in neural information processing systems*, 21, 2008.

[23] Ding Zhou and Xue-Xin Wei. Learning identifiable and interpretable latent models of high-dimensional neural activity using pi-vae. *Advances in Neural Information Processing Systems*, 33:7234–7247, 2020.

[24] Diederik P Kingma and Max Welling. Auto-encoding variational bayes. *arXiv preprint arXiv:1312.6114*, 2013.

[25] Ramon Nogueira, Chris C Rodgers, Randy M Bruno, and Stefano Fusi. The geometry of cortical representations of touch in rodents. *Nature Neuroscience*, pages 1–12, 2023.

[26] Mark M Churchland, Byron M Yu, John P Cunningham, Leo P Sugrue, Marlene R Cohen, Greg S Corrado, William T Newsome, Andrew M Clark, Paymon Hosseini, Benjamin B Scott, et al. Stimulus onset quenches neural variability: a widespread cortical phenomenon. *Nature neuroscience*, 13(3):369–378, 2010.

[27] Gamaleldin F Elsayed, Antonio H Lara, Matthew T Kaufman, Mark M Churchland, and John P Cunningham. Reorganization between preparatory and movement population responses in motor cortex. *Nature communications*, 7(1):1–15, 2016.

[28] Adam G Rouse and Marc H Schieber. Condition-dependent neural dimensions progressively shift

during reach to grasp. *Cell reports*, 25(11):3158–3168, 2018.

[29] Xiyuan Jiang, Hemant Saggar, Stephen I Ryu, Krishna V Shenoy, and Jonathan C Kao. Structure in neural activity during observed and executed movements is shared at the neural population level, not in single neurons. *Cell reports*, 32(6):108006, 2020.

[30] Dimitri Yatsenko, Krešimir Josić, Alexander S Ecker, Emmanouil Froudarakis, R James Cotton, and Andreas S Tolias. Improved estimation and interpretation of correlations in neural circuits. *PLoS computational biology*, 11(3):e1004083, 2015.

[31] Nandakumar S Narayanan, Eyal Y Kimchi, and Mark Laubach. Redundancy and synergy of neuronal ensembles in motor cortex. *Journal of Neuroscience*, 25(17):4207–4216, 2005.

[32] Guanghao Sun, Fei Zeng, Michael McCartin, Qiaosheng Zhang, Helen Xu, Yaling Liu, Zhe Sage Chen, and Jing Wang. Closed-loop stimulation using a multiregion brain-machine interface has analgesic effects in rodents. *Science Translational Medicine*, 14(651):eabm5868, 2022.

[33] Jinyong Zhang, Ryan N Hughes, Namsoo Kim, Isabella P Fallon, Konstantin Bakhurin, Jiwon Kim, Francesco Paolo Ulloa Severino, and Henry H Yin. A one-photon endoscope for simultaneous patterned optogenetic stimulation and calcium imaging in freely behaving mice. *Nature Biomedical Engineering*, pages 1–12, 2022.

[34] Dmitry Kobak, Wieland Brendel, Christos Constantinidis, Claudia E Feierstein, Adam Kepecs, Zachary F Mainen, Xue-Lian Qi, Ranulfo Romo, Naoshige Uchida, and Christian K Machens. Demixed principal component analysis of neural population data. *Elife*, 5:e10989, 2016.

[35] Simon Musall, Matthew T Kaufman, Ashley L Juavinett, Steven Gluf, and Anne K Churchland. Single-trial neural dynamics are dominated by richly varied movements. *Nature neuroscience*, 22(10):1677–1686, 2019.

[36] Edgar Y Walker, R James Cotton, Wei Ji Ma, and Andreas S Tolias. A neural basis of probabilistic computation in visual cortex. *Nature Neuroscience*, 23(1):122–129, 2020.

[37] Ashesh K Dhawale, Maurice A Smith, and Bence P Ölveczky. The role of variability in motor learning. *Annual review of neuroscience*, 40:479, 2017.

[38] Patrick T Sadtler, Kristin M Quick, Matthew D Golub, Steven M Chase, Stephen I Ryu, Elizabeth C Tyler-Kabara, Byron M Yu, and Aaron P Batista. Neural constraints on learning. *Nature*, 512(7515):423–426, 2014.

[39] Jay A Hennig, Emily R Oby, Matthew D Golub, Lindsay A Bahureksa, Patrick T Sadtler, Kristin M Quick, Stephen I Ryu, Elizabeth C Tyler-Kabara, Aaron P Batista, Steven M Chase, et al. Learning is shaped by abrupt changes in neural engagement. *Nature Neuroscience*, 24(5):727–736, 2021.

[40] Ege Altan, Sara A Solla, Lee E Miller, and Eric J Perreault. Estimating the dimensionality of the manifold underlying multi-electrode neural recordings. *PLoS computational biology*, 17(11):e1008591, 2021.

[41] Jose M Carmena, Mikhail A Lebedev, Craig S Henriquez, and Miguel AL Nicolelis. Stable ensemble performance with single-neuron variability during reaching movements in primates. *Journal of Neuroscience*, 25(46):10712–10716, 2005.

[42] Jeffrey Alstott, Michael Breakspear, Patric Hagmann, Leila Cammoun, and Olaf Sporns. Modeling the impact of lesions in the human brain. *PLoS computational biology*, 5(6):e1000408, 2009.

[43] Juan A Gallego, Matthew G Perich, Lee E Miller, and Sara A Solla. Neural manifolds for the control of movement. *Neuron*, 94(5):978–984, 2017.

[44] Yuke Yan, James M Goodman, Dalton D Moore, Sara A Solla, and Sliman J Bensmaia. Unexpected complexity of everyday manual behaviors. *Nature communications*, 11(1):1–8, 2020.

[45] Najib J Majaj, Ha Hong, Ethan A Solomon, and James J DiCarlo. Simple learned weighted sums of inferior temporal neuronal firing rates accurately predict human core object recognition performance. *Journal of Neuroscience*, 35(39):13402–13418, 2015.

[46] Marino Pagan, Luke S Urban, Margot P Wohl, and Nicole C Rust. Signals in inferotemporal and perirhinal cortex suggest an untangling of visual target information. *Nature neuroscience*, 16(8):1132–1139, 2013.

[47] David M Schneider, Janani Sundararajan, and Richard Mooney. A cortical filter that learns to suppress the acoustic consequences of movement. *Nature*, 561(7723):391–395, 2018.

[48] Fang Wang, Yiwen Wang, Kai Xu, Hongbao Li, Yuxi Liao, Qiaosheng Zhang, Shaomin Zhang, Xiaoxiang Zheng, and José C Principe. Quantized attention-gated kernel reinforcement learning for brain–machine interface decoding. *IEEE transactions on neural networks and learning systems*, 28(4):873–886, 2015.

[49] Eva L Dyer, Mohammad Gheshlaghi Azar, Matthew G Perich, Hugo L Fernandes, Stephanie Naufel, Lee E Miller, and Konrad P Körding. A cryptography-based approach for movement decoding. *Nature biomedical engineering*, 1(12):967–976, 2017.

[50] Joseph E O'Doherty, MMB Cardoso, JG Makin, and PN Sabes. Nonhuman primate reaching with multichannel sensorimotor cortex electrophysiology. *Zenodo http://doi. org/10.5281/zenodo*, 583331, 2017.

Acknowledgements

We would like to thank Yuxiao Yang, and Huaqin Sun for valuable discussions. This work was partly supported by grants from the National Key R&D Program of China (2018YFA0701400), Key R&D Program of Zhejiang (no. 2022C03011), the Chuanqi Research and Development Center of Zhejiang University, the Starry Night Science Fund of Zhejiang University Shanghai Institute for Advanced Study (SN-ZJU-SIAS-002), the Fundamental Research Funds for the Central Universities.

Author contributions

Y.G.L. conceived the study, designed the experiments, analyzed the data, and wrote the manuscript. X.Y.Z designed correlation analysis experiments and modified the manuscript. Y.M.W. and Y.Q. supervised this study.

Competing interests

The authors declare no competing interests.

Supplementary Information

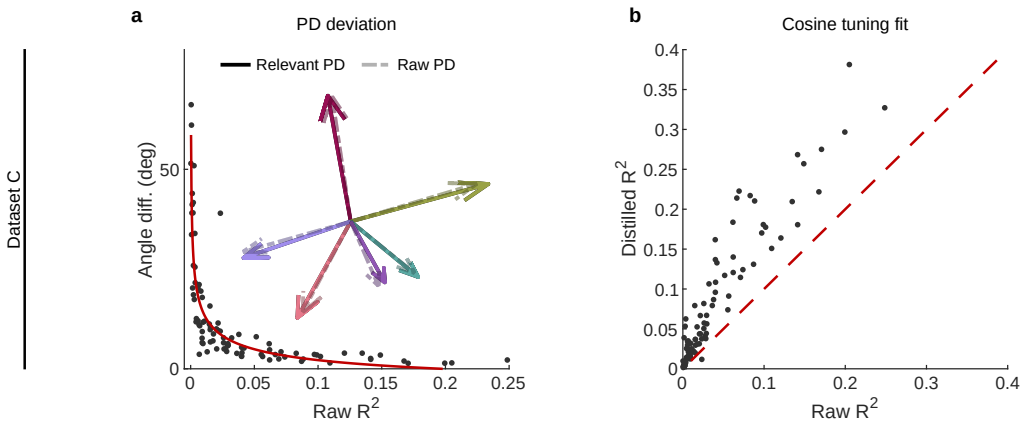

Figure S1: **The effect of irrelevant signals on relevant signals at the single-neuron level. a,b** Same as Fig. 3, but for dataset C. **a**, The angle difference (AD) of preferred direction (PD) between raw and distilled signals as a function of the R^2 of raw signals. Each black point represents a neuron (n=91). The red curve is the fitting curve between R^2 and AD. Five example larger R^2 neurons' PDs are shown in the inset plot, where the solid line arrows represent the PD of relevant signals, and the dotted line arrows represent the PDs of raw signals. **b**, Comparison of the cosine tuning fit (R^2) before and after distillation of single neurons (black points), where the x-axis and y-axis represent neurons' R^2 of raw and distilled signals.

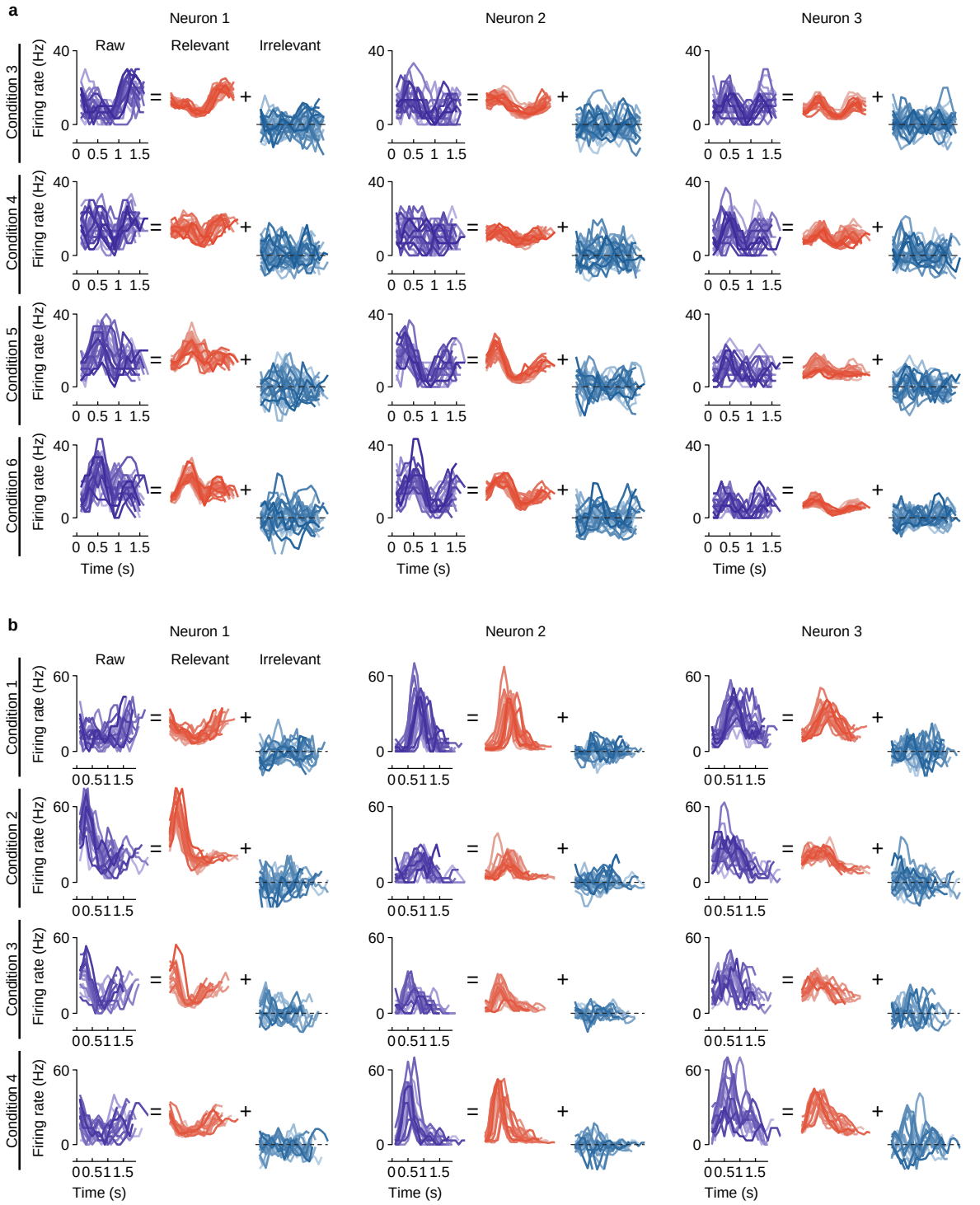

Figure S2: **The firing activity of example neurons. a**, Example of three neurons' raw firing activity decomposed into task-relevant and irrelevant parts using all trials in held-out test sets for four conditions (4 of 8 directions) of center-out reaching task. **b**, Example of three neurons' raw firing activity decomposed into task-relevant and irrelevant parts using all trials in held-out test sets for four conditions (4 of 12 conditions) of obstacle avoidance task.

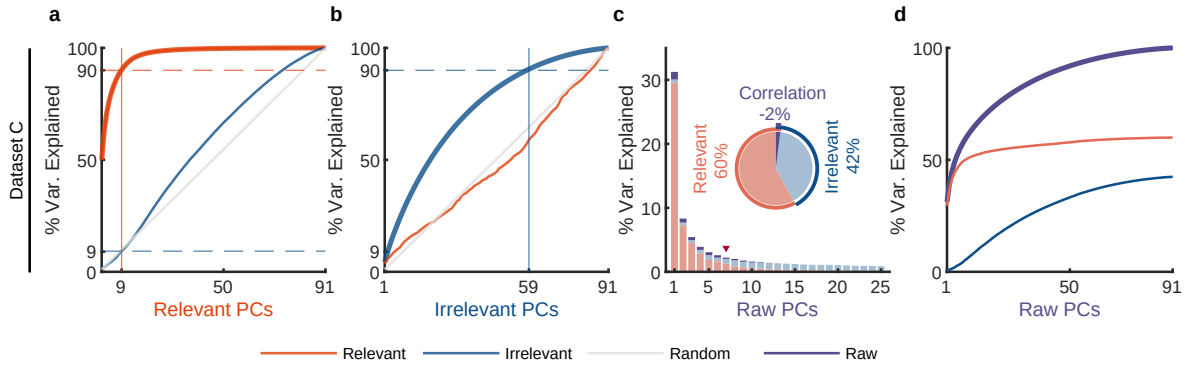

Figure S3: **The effect of irrelevant signals on analyzing neural activity at the population level.** **a-d**, Same as Fig. 4, but for dataset C. **a,b**, PCA is separately applied on relevant and irrelevant signals to get relevant PCs and irrelevant PCs. The thick lines represent the cumulative variance explained for the signals on which PCA has been performed, while the thin lines represent the variance explained by those PCs for other signals. Red, blue, and gray colors indicate relevant signals, irrelevant signals, and random Gaussian noise (for chance level). The cumulative variance explained for task-relevant (**a**) and irrelevant (**b**) signals got by d-VAE. **c,d**, PCA is applied on raw signals to get raw PCs. **c**, The bar plot represents the composition of each raw PC. The inset pie plot shows the overall proportion of raw signals, where red, blue, and purple colors indicate relevant signals, irrelevant signals, and the correlation between relevant and relevant signals. The PC marked with a red triangle indicates the last PC where the variance of relevant signals is greater than or equal to that of irrelevant signals. **d**, The cumulative variance explained by raw PCs for different signals, where the thick lines represent the cumulative variance explained for raw signals(purple), while the thin lines represent the variance explained for relevant (red) and irrelevant (blue) signals.

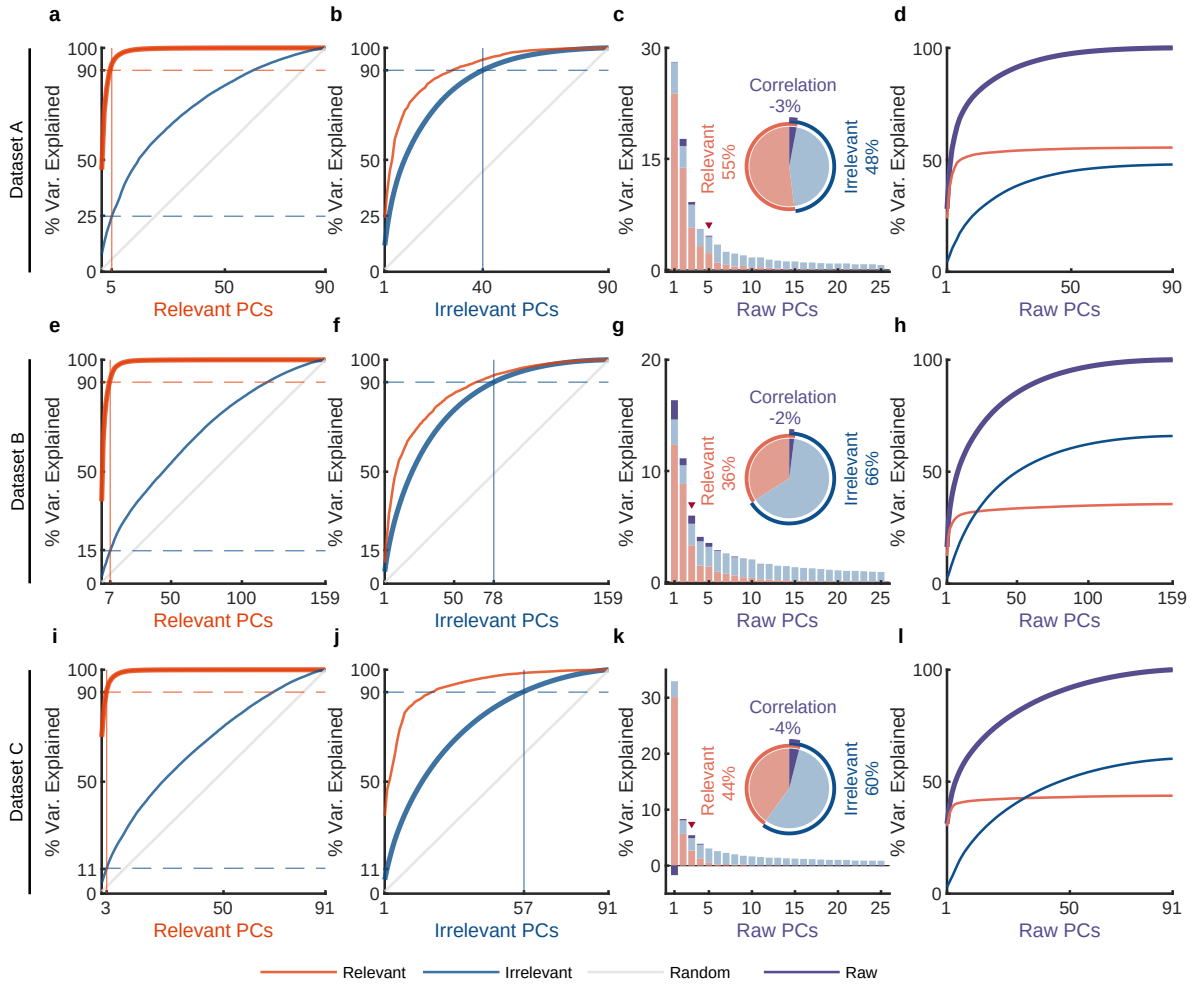

Figure S4: **The effect of irrelevant signals obtained by pi-VAE on analyzing neural activity at the population level. a-l**, Same as Fig. 4 and Fig. S3, but for pi-VAE. **a,b**, PCA is separately applied on relevant and irrelevant signals to get relevant PCs and irrelevant PCs. The thick lines represent the cumulative variance explained for the signals on which PCA has been performed, while the thin lines represent the variance explained by those PCs for other signals. Red, blue, and gray colors indicate relevant signals, irrelevant signals, and random Gaussian noise (for chance level). The cumulative variance explained for task-relevant (**a**) and irrelevant (**b**) signals on dataset A. **c,d**, PCA is applied on raw signals to get raw PCs. **c**, The bar plot represents the composition of each raw PC. The inset pie plot shows the overall proportion of raw signals, where red, blue, and purple colors indicate relevant signals, irrelevant signals, and the correlation between relevant and relevant signals. The PC marked with a red triangle indicates the last PC where the variance of relevant signals is greater than or equal to that of irrelevant signals. **d**, The cumulative variance explained by raw PCs for different signals, where the thick line represents the cumulative variance explained for raw signals(purple), while the thin line represents the variance explained for relevant (red) and irrelevant (blue) signals. **e-h, i-l**, Same as **a-d**, but for datasets B and C.

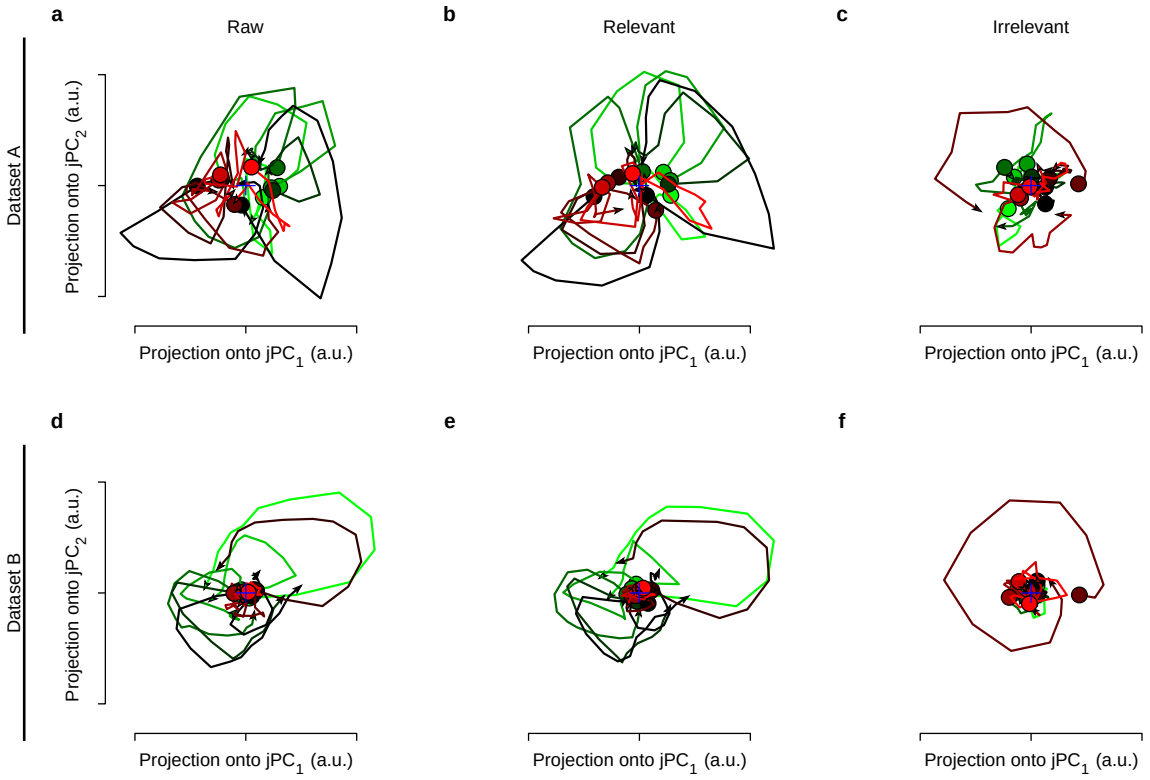

Figure S5: **The rotational dynamics of raw, relevant, and irrelevant signals.** datasets A and B have twelve and eight conditions, respectively. We get the trial-averaged neural responses for each condition, then apply jPCA to raw, relevant, and irrelevant signals to get the top two jPC, respectively. **a**, The rotational dynamics of raw neural signals. **b**, The rotational dynamics of relevant signals obtained by d-VAE. **c**, The rotational dynamics of irrelevant signals obtained by d-VAE. We can see that the rotational dynamics of task-relevant signals are similar to that of raw signals, but the rotational dynamics of task-irrelevant signals are irregular. **d-f**, Same as **a-c**, but for dataset B.

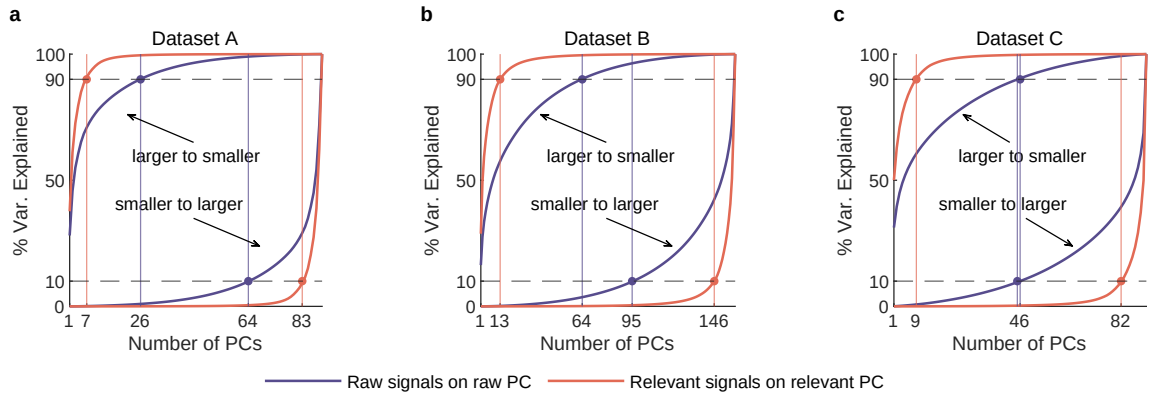

Figure S6: **The cumulative variance of raw and task-relevant signals.** **a**, PCA is applied separately on raw and distilled task-relevant signals to get raw PCs and relevant PCs. The cumulative variance of raw (purple) and task-relevant signals (red) on dataset A (n=90). Two upper left corner curves denote the variance accumulation from larger to smaller variance PCs. Two lower right corner curves indicate accumulation from smaller to larger variance PCs. The horizontal lines represent the 10%, and 90% variance explained. The vertical lines indicate the number of dimensions accounted for the last 10% and top 90% of the variance of task-relevant (red) and raw (purple) signals. Here we call the subspace composed by PCs of capturing top 90% variance the primary subspace, and the subspace composed by PCs of capturing last 10% variance the secondary subspace. We can see that the dimensionality of the primary subspace of raw signals is significantly higher than that of relevant signals, indicating that irrelevant signals make us overestimate the dimensionality of specific tasks. **b,c**, Same as **a**, but for datasets B (n=159) and C (n=91).

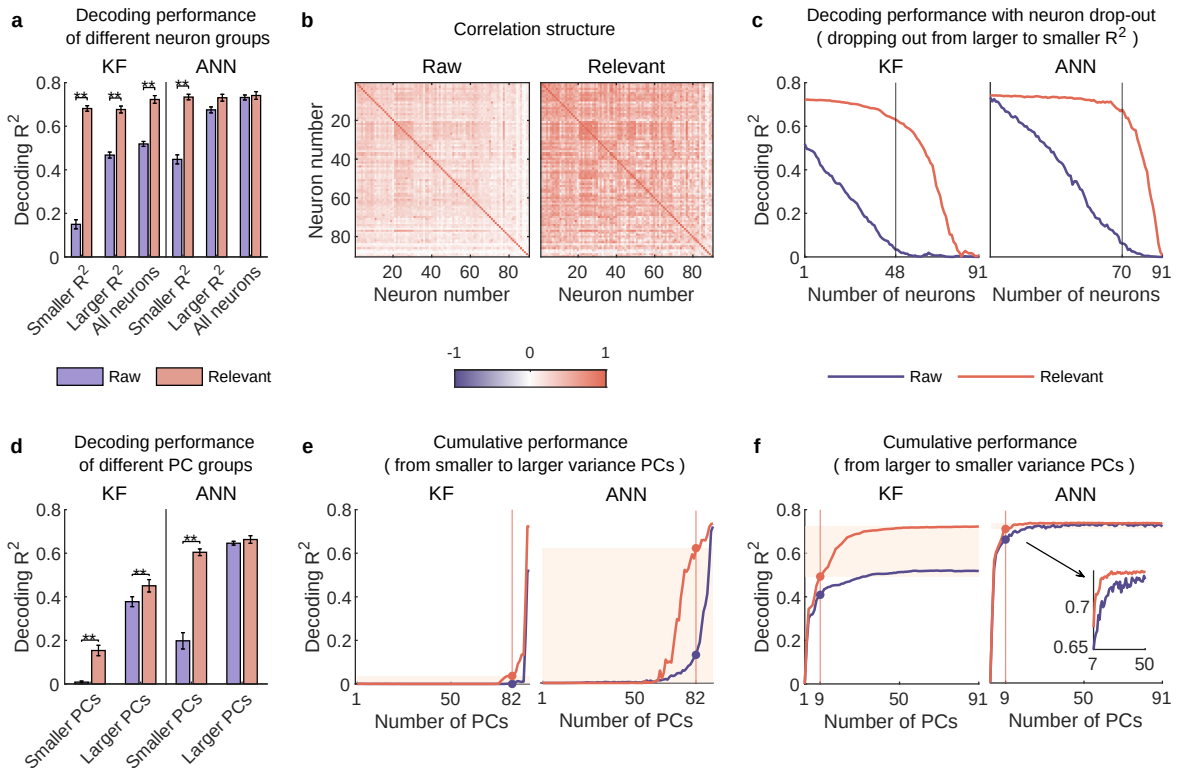

Figure S7: **trivial neural activities encode rich task information in complex nonlinear ways. a-c**, Same as Fig. 5, but for dataset C (n=91). **d-f**, Same as Fig. 6, but for dataset C. **a**, The comparison of decoding performance between raw (purple) and distilled signals (red) with different neuron groups, including smaller R^2 neuron ($R^2 <= 0.03$), larger R^2 neuron ($R^2 > 0.03$), and all neurons. Error bars indicate mean $\pm$ SD across cross-validation folds. Asterisks denote significance of Wilcoxon rank-sum test with $^{\star}P < 0.05$, $^{\star\star}P < 0.01$. **b**, The correlation matrix of all neurons of raw and task-relevant signals. **c**, The decoding performance of KF (left) and ANN (right) with neurons dropped out from larger to smaller R^2. The vertical gray lines indicate the number of dropped neurons at which raw and task-relevant signals have the greatest performance difference. **d**, The comparison of decoding performance between raw (purple) and distilled signals (red) composed of different raw-PC groups, including smaller variance PCs (the proportion of irrelevant signals that make up raw PCs is higher than that of relevant signals), larger variance PCs (the proportion of irrelevant signals is lower than that of relevant ones). Error bars indicate mean $\pm$ s.d. across five cross-validation folds. Asterisks denote significance of Wilcoxon rank-sum test with $^{\star}P < 0.05$, $^{\star\star}P < 0.01$. **e**, The cumulative decoding performance of signals composed of cumulative PCs that are ordered from smaller to larger variance using KF (left) and ANN (right). The red patches indicate the decoding ability of the last 10% variance of relevant signals. **f**, Same as **e**, but PCs are ordered from larger to smaller variance. The red patches indicate the decoding gain of the last 10% variance signals of relevant signals superimposing on their top 90% variance signals.

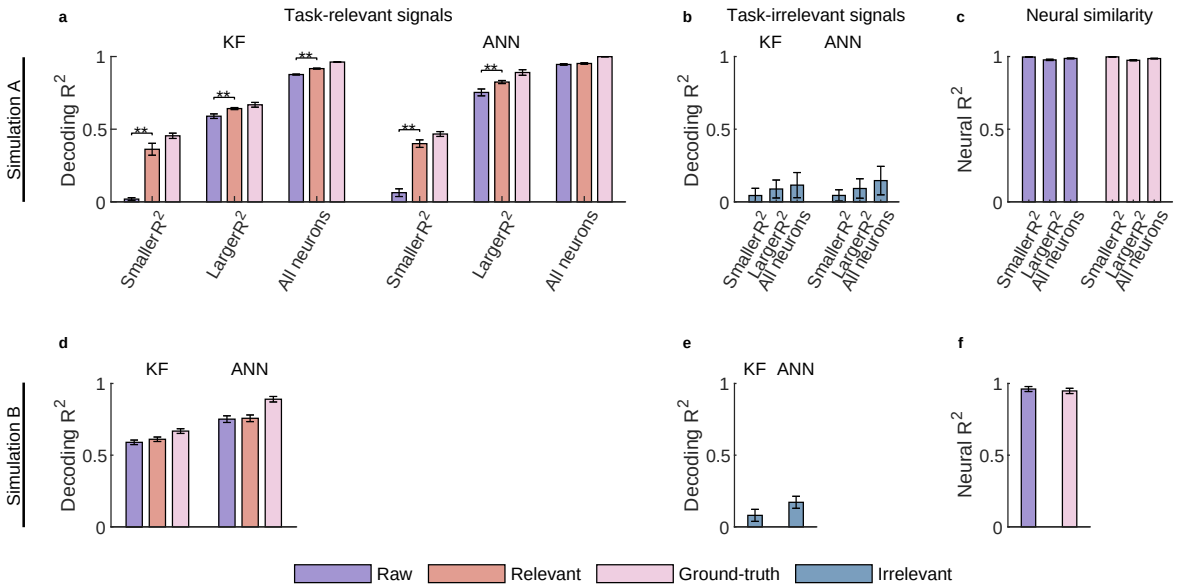

Figure S8: **Simulation results. a-c**, The simulation dataset A simulated a situation where the smaller R^2 neurons contain a certain amount of task information, but the task information cannot be decoded from these neurons due to being covered by noise. We used this experiment to demonstrate that d-VAE can utilize the larger R^2 neurons to help the smaller R^2 neurons restore their original face. **a**, The comparison of decoding performance between raw (purple), distilled (red) and ground-truth (pink) signals with different neuron groups, including smaller R^2 neuron ($R^2 <= 0.03$), larger R^2 neuron ($R^2 > 0.03$), and all neurons. Error bars indicate mean ± s.d. (n=5 folds). Asterisks denote significance of Wilcoxon rank-sum test with $^{**}P < 0.01$. **b**, The decoding performance of task-irrelevant signals got by d-VAE with different neuron groups. Error bars indicate mean ± s.d. (n=5 folds). **c**, The neural similarity between distilled task-relevant (red) and raw signals (purple) and between relevant and ground-truth signals (pink) with different neuron groups. Error bars indicate mean ± s.d. (n=5 folds). **d-f**, The simulation dataset B simulated the situation where linear decoding is significantly inferior to nonlinear decoding. We used this experiment to demonstrate that d-VAE can not make the linear decoder achieve similar performance as the nonlinear decoder. **d**, The comparison of decoding performance between raw (purple), relevant (red), and ground-truth (pink) signals. Error bars indicate mean ± s.d. (n=5 folds). **e**, The decoding performance of task-irrelevant signals got by d-VAE. Error bars indicate mean ± s.d. (n=5 folds). **f**, The neural similarity between distilled task-relevant (red) and raw signals (purple) and between relevant and ground-truth signals (pink). Error bars indicate mean ± s.d. (n=5 folds).

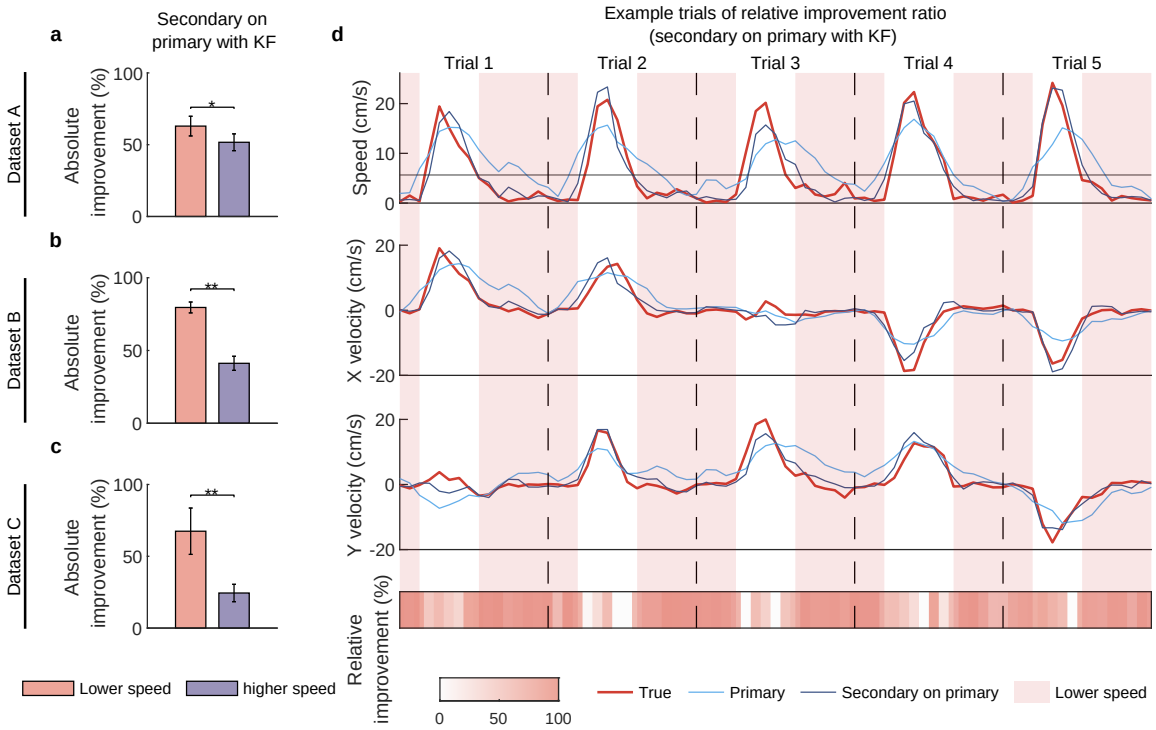

Figure S9: **Smaller variance PC signals preferentially improve lower-speed velocity. a**, The comparison of absolute improvement ratio between lower-speed (red) and higher-speed (purple) velocity when superimposing secondary signals on primary signals with KF on dataset A. Error bars indicate mean ± s.d. across five cross-validation folds. Asterisks denote significance of Wilcoxon rank-sum test with $^{\star}P < 0.05$, $^{\star\star}P < 0.01$. **b, c**, Same as **a**, but for datasets B and C. **d**, The comparison of relative improvement ratio between lower-speed (red patch) and higher-speed (no patch) velocity when superimposing secondary signals on primary signals with KF on dataset B. The first-row plot shows five example trials' speed profile of the decoded velocity using primary signals (light blue line) and full signals (dark blue line; superimposing secondary signals on primary signals) and the true velocity (red line). The black horizontal line denotes the speed threshold. The second and third-row plots are the same as the first-row plot, but for X and Y velocity. The fourth-row plot shows the relative improvement ratio for each point in trials.